Arbitrary order exactly divergence-free central discontinuous Galerkin methods for ideal MHD equations

Fengyan Li *, Liwei Xu

Department of Mathematical Sciences, Rensselaer Polytechnic Institute, Troy, NY 12180-3590, United States

ABSTRACT

Ideal magnetohydrodynamic (MHD) equations consist of a set of nonlinear hyperbolic conservation laws, with a divergence-free constraint on the magnetic field. Neglecting this constraint in the design of computational methods may lead to numerical instability or nonphysical features in solutions. In our recent work [F. Li, L. Xu, S. Yakovlev, Central discontinuous Galerkin methods for ideal MHD equations with the exactly divergence-free magnetic field, Journal of Computational Physics 230 (2011) 4828–4847], second and third order exactly divergence-free central discontinuous Galerkin methods were proposed for ideal MHD equations. In this paper, we further develop such methods with higher order accuracy. The novelty here is that the well-established *H*(div)-conforming finite element spaces are used in the constrained transport type framework, and the magnetic induction equations are extensively explored in order to extract sufficient information to uniquely reconstruct an exactly divergence-free magnetic field. The overall algorithm is local, and it can be of *arbitrary* order of accuracy. Numerical examples are presented to demonstrate the performance of the proposed methods especially when they are fourth order accurate.

© 2011 Elsevier Inc. All rights reserved.

1. Introduction

In this paper, we continue our recent development in [20] to devise exactly divergence-free numerical methods for ideal magnetohydrodynamic (MHD) equations. These equations arise in many areas in physics and engineering, and they consist of a set of nonlinear hyperbolic conservation laws, with a divergence-free constraint on the magnetic field. Though this constraint holds for the exact solution as long as it does initially, neglecting this condition in the design of computational algorithms may lead to numerical instability or nonphysical features of approximating solutions [17,7,15,5,30,14,19,6,21,4].

In [20], exactly divergence-free central discontinuous Galerkin (DG) methods with second and third order accuracy were developed for ideal MHD equations. The methods are based on the central DG methods in [24,25] and use a different discretization for magnetic induction equations. More specifically, while other conservative quantities are evolved with central DG methods of [24], the magnetic field (or its two components in two dimensions) is updated such that its normal component is first approximated by discretizing magnetic induction equations on interfaces of mesh elements, and then an element-by-element divergence-free reconstruction procedure follows with compatible accuracy. This gives numerical methods with exactly divergence-free magnetic fields, and these methods demonstrate good performance in both accuracy and stability. On the other hand, such reconstruction by matching the pre-computed normal component of the magnetic field at mesh interfaces is under-determined for higher order accuracy. In this paper, a new strategy is proposed. In particular, we extensively explore the magnetic induction equations to extract sufficient information about the magnetic field, with which an element-

* Corresponding author.
  E-mail addresses: lif@rpi.edu (F. Li), xul3@rpi.edu (L. Xu).

by-element reconstruction is defined. We prove that the reconstruction is uniquely determined, and the resulting magnetic field is exactly divergence-free with *arbitrary* order of (formal) accuracy. In addition, when being second or third order accurate, the proposed method is the same as that in [20]. Numerical experiments are carried out to illustrate the performance of the overall algorithms when they are fourth order accurate. The methods are presented for two dimensions in this paper, and there is no difficulty to extend them to three dimensions.

Our work is inspired by the development of H(div)-conforming finite element spaces [8,9] in classical finite element methods. A finite element space is said to be H(div)-conforming if its function is piecewise smooth (such as being piecewise polynomials) and its normal component is continuous across mesh element interfaces. Though some of such spaces have been used in the design of exactly divergence-free numerical methods for ideal MHD equations [2,21,4,22] (also see Section 5.2 for more discussion), to our best knowledge, the proposed methods are the first to utilize the established results and analysis techniques for H(div)-conforming finite element spaces to systematically design exactly divergence-free numerical methods of any order of accuracy for MHD simulations. Not like in standard Galerkin type methods using such spaces, the proposed local procedure does not involve inverting a global mass matrix.

The proposed methods can be regarded as constrained transport type methods (see, e.g. [15,5,16,21]), with central DG methods of [24] as the base method and a new divergence-free reconstruction strategy. A basic idea of constrained transport methods is to work with the magnetic induction system in its integral form along element boundaries. To achieve higher order accuracy in our proposed methods, we further explore the magnetic induction equations in order to extract more information about the magnetic field. Central DG methods are a family of high order numerical methods defined on overlapping meshes with two sets of numerical solutions. Compared with standard DG methods [11,19] which are defined on a single mesh with one numerical solution and therefore are more efficient in memory usage, central DG methods do not explicitly use any numerical flux (which is exact or approximate Riemann solver), and the time step allowed for linear stability is larger when the accuracy of the methods is higher than one [25,20]. Moreover, no averaging or interpolation step is needed for our proposed methods to produce a single-valued electric field flux at grid-points. Such step is inherent in our central framework on overlapping meshes, and it is required explicitly for Godunov type constrained transport methods [16,4] to define an exactly divergence-free reconstruction, and for this, upwind mechanism needs to be incorporated due to the stability consideration especially for high order accuracy.

The remainder of the paper is organized as follows. In Section 2, we describe the governing equations and introduce notations for meshes and discrete spaces. In Section 3, exactly divergence-free central DG methods are proposed for ideal MHD equations, and the main theorem is stated for a local reconstruction procedure, with its proof given in Section 4. In Section 5, further discussions are made on divergence-free discrete spaces, relations of the proposed methods to some other divergence-free methods, high order time discretizations, and nonlinear limiters. Numerical examples are reported in Section 6, followed by concluding remarks in Section 7. In Appendix A, the definition of the divergence-free reconstruction in [20] is given for the reference purpose. We include in Appendix B the formulas of the fourth order reconstruction proposed in this paper.

2. Preliminaries: equations and notations

Consider the ideal MHD equations, which are a hyperbolic system

$$\frac{\partial \rho}{\partial t} + \nabla \cdot (\rho \mathbf{u}) = 0, \tag{1}$$

$$\frac{\partial (\rho \mathbf{u})}{\partial t} + \nabla \cdot \left[\rho \mathbf{u}\mathbf{u}^{\mathrm{T}} + \left(p + \frac{1}{2}|\mathbf{B}|^2 \right)\mathbf{I} - \mathbf{B}\mathbf{B}^{\mathrm{T}} \right] = 0, \tag{2}$$

$$\frac{\partial \mathbf{B}}{\partial t} - \nabla \times (\mathbf{u} \times \mathbf{B}) = 0, \tag{3}$$

$$\frac{\partial \mathcal{E}}{\partial t} + \nabla \cdot \left[\left(\mathcal{E} + p + \frac{1}{2}|\mathbf{B}|^2 \right)\mathbf{u} - \mathbf{B}(\mathbf{u} \cdot \mathbf{B}) \right] = 0, \tag{4}$$

with a divergence-free constraint

$$\nabla \cdot \mathbf{B} = 0. \tag{5}$$

Here ρ is the density, p is the hydrodynamic pressure, $\mathbf{u} = (u_x, u_y, u_z)^{\mathrm{T}}$ is the velocity field, and $\mathbf{B} = (B_x, B_y, B_z)^{\mathrm{T}}$ is the magnetic field. The total energy $\mathcal{E}$ is given by $\mathcal{E} = \frac{1}{2}\rho|\mathbf{u}|^2 + \frac{1}{2}|\mathbf{B}|^2 + \frac{p}{\gamma-1}$ with γ as the ratio of the specific heats. We use the superscript T to denote the vector transpose. In addition, $\mathbf{I}$ is the identity matrix, $\nabla \cdot$ is the divergence operator, and $\nabla \times$ is the curl operator. Eqs. (1), (2), and (4) are from the conservation of mass, momentum, and energy, and (3) is the magnetic induction equation system. In two dimensions when all unknown functions depend only on spatial variables x and y, Eqs. (1)–(4) can be rewritten as

$$\frac{\partial \mathbf{U}}{\partial t} + \frac{\partial}{\partial x}\mathbf{F}_1(\mathbf{U}, \mathcal{B}) + \frac{\partial}{\partial y}\mathbf{F}_2(\mathbf{U}, \mathcal{B}) = 0, \tag{6}$$

$$\frac{\partial \mathcal{B}}{\partial t} + \hat{\nabla} \times E_z(\mathbf{U}, \mathcal{B}) = 0, \tag{7}$$

where $\mathbf{U} = (\rho, \rho u_x, \rho u_y, \rho u_z, B_z, \mathcal{E})^{\mathrm{T}}$, $\mathcal{B} = (B_x, B_y)^{\mathrm{T}}$, and

$$\mathbf{F}_1(\mathbf{U}, \mathcal{B}) = \left(\rho u_x, \rho u_x^2 + p + \frac{1}{2}|\mathbf{B}|^2 - B_x^2, \rho u_x u_y - B_x B_y, \rho u_x u_z - B_x B_z, u_x B_z - u_z B_x, u_x\left(\mathcal{E} + p + \frac{1}{2}|\mathbf{B}|^2\right) - B_x(\mathbf{u} \cdot \mathbf{B})\right)^{\mathrm{T}}, \qquad (8)$$

$$\mathbf{F}_2(\mathbf{U}, \mathcal{B}) = \left(\rho u_y, \rho u_y u_x - B_y B_x, \rho u_y^2 + p + \frac{1}{2}|\mathbf{B}|^2 - B_y^2, \rho u_y u_z - B_y B_z, u_y B_z - u_z B_y, u_y\left(\mathcal{E} + p + \frac{1}{2}|\mathbf{B}|^2\right) - B_y(\mathbf{u} \cdot \mathbf{B})\right)^{\mathrm{T}}. \qquad (9)$$

In addition, $E_z(\mathbf{U}, \mathcal{B}) = u_y B_x - u_x B_y$, and it is the z-component of the electric field $\mathbf{E} = -\mathbf{u} \times \mathbf{B}$. We also use $\hat{\nabla} \times E_z = \left(\frac{\partial E_z}{\partial y}, -\frac{\partial E_z}{\partial x}\right)^{\mathrm{T}}$, which gives the first two components of $\nabla \times (0, 0, E_z)^{\mathrm{T}}$. Note that B_z does not contribute to $\nabla \cdot \mathbf{B}$ in two dimensions, therefore for convenience we call $\mathcal{B}$ the magnetic field and (7) the magnetic induction system from now on.

Next, we introduce notations used in numerical schemes. Since only Cartesian grids are considered in this paper, we assume the computational domain is $\Omega = (x_{\min}, x_{\max}) \times (y_{\min}, y_{\max}) \subset \mathbb{R}^d$, with $d = 2$. Let $\{x_i\}_i$ and $\{y_j\}_j$ be partitions of $(x_{\min}, x_{\max})$ and $(y_{\min}, y_{\max})$, respectively, and $x_{i+\frac{1}{2}} = \frac{1}{2}(x_i + x_{i+1})$ and $y_{j+\frac{1}{2}} = \frac{1}{2}(y_j + y_{j+1})$. Then $\mathcal{T}_h^C = \{C_{i,j}, \forall i,j\}$ and $\mathcal{T}_h^D = \{D_{i,j}, \forall i,j\}$ define two overlapping meshes for Ω, with $C_{i,j} = (x_i, x_{i+1}) \times (y_j, y_{j+1})$ and $D_{i,j} = (x_{i-\frac{1}{2}}, x_{i+\frac{1}{2}}) \times (y_{j-\frac{1}{2}}, y_{j+\frac{1}{2}})$. They are also called primal and dual meshes, respectively. Discrete spaces will be defined associated with each mesh. In the numerical methods introduced in next section, different strategies are used to approximate $\mathbf{U}$ and $\mathcal{B}$. For $\mathbf{U}$, we use a piecewise polynomial vector space $\mathcal{U}_h^{\star,k}$ as the discrete space, that is,

$$\mathcal{U}_h^{\star,k} = \left\{\mathbf{v} : \mathbf{v}|_K \in [P^k(K)]^{8-d}, \forall K \in \mathcal{T}_h^\star\right\}, \qquad (10)$$

where $P^k(K)$ denotes the space of polynomials in K with the total degree at most k, and $[P^k(K)]^r = \{\mathbf{v} = (v_1, \ldots, v_r)^{\mathrm{T}} : v_i \in P^k(K), i = 1, \ldots, r\}$ is its vector version with any positive integer r. Here and below $\star$ denotes C or D. For the magnetic field $\mathcal{B}$, we want to approximate it by a piecewise polynomial vector field which is exactly divergence-free. Such function is characterized by its being piecewise divergence-free, and its normal component being continuous across mesh elements. Motivated by the development of classical finite elements on Cartesian meshes, we take the following $\mathcal{M}_h^{\star,k}$ as the discrete space for $\mathcal{B}$,

$$\mathcal{M}_h^{\star,k} = \left\{\mathbf{v} \in H(\mathrm{div}^0; \Omega) : \mathbf{v}|_K \in \mathcal{W}^k(K), \forall K \in \mathcal{T}_h^\star\right\} = \{\mathbf{v} : \mathbf{v}|_K \in \mathcal{W}^k(K), \nabla \cdot \mathbf{v}|_K = 0, \forall K \in \mathcal{T}_h^\star, \text{and the normal component of}$$

$$\mathbf{v} \text{ is continuous across each mesh element interface}\}, \qquad (11)$$

with $\mathcal{W}^k(K)$ being an augmented space of the polynomial vector space of degree k,

$$\mathcal{W}^k(K) = [P^k(K)]^d \oplus \mathrm{span}\{\hat{\nabla} \times (x^{k+1}y), \hat{\nabla} \times (xy^{k+1})\} = \{\mathbf{v} : \mathbf{v} = \mathbf{u} + a\hat{\nabla} \times (x^{k+1}y) + b\hat{\nabla} \times (xy^{k+1}), \forall \mathbf{u}$$

$$\in [P^k(K)]^d, \forall a, b \in \mathbb{R}\}. \qquad (12)$$

In fact, $\mathcal{M}_h^{\star,k}$ is the divergence-free subspace of the following Brezzi–Douglas–Marini (BDM) finite element space,

$$\mathrm{BDM}_k^\star = \left\{\mathbf{v} \in H(\mathrm{div}; \Omega) : \mathbf{v}|_K \in \mathcal{W}^k(K), \forall K \in \mathcal{T}_h^\star\right\},$$

$$= \{\mathbf{v} : \mathbf{v}|_K \in \mathcal{W}^k(K), \forall K \in \mathcal{T}_h^\star, \text{and the normal component of } \mathbf{v} \text{ is continuous across each mesh element interface}\}, \qquad (13)$$

which is one of the widely used $H(\mathrm{div})$-conforming finite element spaces and was introduced in [8] to solve second order elliptic problems in their first order form. Moreover, $\mathcal{M}_h^{\star,k}$ has optimal approximation properties for exactly divergence-free smooth functions on Cartesian meshes with respect to index k (see Lemma 2.1 in [8]). Though the building block $\mathcal{W}^k(K)$ is an augmented space of a polynomial vector space, the added part, $\mathrm{span}\{\hat{\nabla} \times (x^{k+1}y), \hat{\nabla} \times (xy^{k+1})\}$, will not contribute to the divergence of a function in $\mathcal{W}^k(K)$. This is stated below together with another property of $\mathcal{W}^k(K)$ we will use later. They can be verified easily based on the definition of $\mathcal{W}^k(K)$.

Lemma 2.1 (Properties of functions in $\mathcal{W}^k$). Given $C = [x_L, x_R] \times [y_L, y_R]$. For any $\mathbf{v} = (v_1, v_2)^{\mathrm{T}} \in \mathcal{W}^k(C)$, there are

Property 1. $v_1(x_\diamond, y) \in P^k(y_L, y_R)$ and $v_2(x, y_\diamond) \in P^k(x_L, x_R)$ for $\diamond = L, R$.

Property 2. $\nabla \cdot \mathbf{v} \in P^{k-1}(C)$.

There are in fact other ways to define the exactly divergence-free discrete space for $\mathcal{B}$, and some examples are given in Section 5. For the numerical algorithm introduced in next section, we need one more discrete space,

$$\mathcal{V}_h^{\star,r} = \left\{\mathbf{v} : \mathbf{v}|_K \in [P^r(K)]^d, \forall K \in \mathcal{T}_h^\star\right\}, \qquad (14)$$

which also consists of piecewise polynomial vector fields. The role of this space will become clear later.

3. Numerical schemes

Though the divergence-free constraint (5) seems to be redundant on the PDE level as it can be derived from the magnetic induction equations with a compatible initial condition, such constraint is not always satisfied by a numerical scheme, and this may lead to nonphysical features of approximating solutions or numerical instability [7,30,19,6]. In this section, we propose central DG methods with an exactly divergence-free magnetic field to solve the system (5)–(7) and therefore (1)–(5). The proposed methods can be of *arbitrary* (at least formal) order of accuracy and they are completely local. In addition, when the accuracy is second or third order, the proposed method is the same as the one developed in [20], and this fact will be established in Theorem 3.1. For simplicity, we present the schemes with the forward Euler method as the time discretization. In Section 5, we comment on higher order temporal accuracy which can be achieved by using strong stability preserving (SSP) high order time discretizations [18]. Such discretizations can also be needed for stability reason (see e.g. Table 6 in [25]).

The proposed methods evolve two copies of numerical solutions, which are assumed to be available at $t = t_n$, denoted as $(\mathbf{U}_h^{n,\star}, \mathcal{B}_h^{n,\star}) \in \mathcal{U}_h^{\star,k} \times \mathcal{M}_h^{\star,k}$ with $\mathcal{B}_h^{n,\star} = \left(B_{x,h}^{n,\star}, B_{y,h}^{n,\star}\right)^{\mathrm{T}}$. Here and below $\star$ denotes C or D. We will describe how to obtain numerical solutions at $t_{n+1} = t_n + \Delta t_n$, denoted as $\left(\mathbf{U}_h^{n+1,\star}, \mathcal{B}_h^{n+1,\star}\right) \in \mathcal{U}_h^{\star,k} \times \mathcal{M}_h^{\star,k}$ with $\mathcal{B}_h^{n+1,\star} = \left(B_{x,h}^{n+1,\star}, B_{y,h}^{n+1,\star}\right)^{\mathrm{T}}$. Due to similarity, we only present the procedure to update $\left(\mathbf{U}_h^{n+1,C}, \mathcal{B}_h^{n+1,C}\right)$.

3.1. Updating $\mathbf{U}_h^{n+1,C}$

To get $\mathbf{U}_h^{n+1,C}$, we apply to (6) the central DG methods of [24] (also see e.g. [20] for a brief review) as the spatial discretization and the forward Euler method as the time discretization. That is, to look for $\mathbf{U}_h^{n+1,C} \in \mathcal{U}_h^{C,k}$ such that for any $\mathbf{V} \in \mathcal{U}_h^{C,k}|_{C_{i,j}} = [P^k(C_{i,j})]^{8-d}$ with any i, j,

$$\int_{C_{i,j}} \mathbf{U}_h^{n+1,C} \cdot \mathbf{V} d\mathbf{x} = \int_{C_{i,j}} \left(\theta_n \mathbf{U}_h^{n,D} + (1 - \theta_n)\mathbf{U}_h^{n,C}\right) \cdot \mathbf{V} d\mathbf{x}$$
$$+ \Delta t_n \left(\int_{C_{i,j}} \left(\mathbf{F}_1^{n,D} \cdot \frac{\partial \mathbf{V}}{\partial x} + \mathbf{F}_2^{n,D} \cdot \frac{\partial \mathbf{V}}{\partial y}\right) d\mathbf{x} - \int_{\partial C_{i,j}} \left(n_1 \mathbf{F}_1^{n,D} + n_2 \mathbf{F}_2^{n,D}\right) \cdot \mathbf{V} ds\right). \tag{15}$$

Here $\theta_n = \Delta t_n / \tau_n \in [0, 1]$, with τ_n being the maximal time step allowed by the CFL restriction [24,20]. $(n_1, n_2)^{\mathrm{T}}$ is the outward pointing unit normal vector along $\partial C_{i,j}$, and $\mathbf{F}_l^{n,D} = \mathbf{F}_l\left(\mathbf{U}_h^{n,D}, \mathcal{B}_h^{n,D}\right)$ for $l = 1, 2$. With two sets of numerical solutions available at time t_n, the methods do not explicitly use numerical fluxes, which are exact or approximate Riemann solvers and are used in Godunov type methods such as standard DG methods [11,19].

3.2. Updating the exactly divergence-free $\mathcal{B}_h^{n+1,C}$

The finite element space $\mathcal{M}_h^{C,k}$ consists of exactly divergence-free vector fields. One can use this space directly in the Galerkin framework to approximate the magnetic field to ensure its zero divergence, see e.g. [10], this however often needs to invert a large mass matrix for each time step (or each inner stage for multi-stage time discretizations). In this paper, we propose a local strategy to obtain an exactly divergence free approximation $\mathcal{B}_h^{n+1,C} = (B_{x,h}^{n+1,C}, B_{y,h}^{n+1,C})^{\mathrm{T}} \in \mathcal{M}_h^{C,k}$. The algorithm is defined element by element and therefore no mass matrix inversion is involved.

Note that an exactly divergence-free vector field is characterized by its continuous normal component across element interfaces and its divergence-free restriction inside each mesh element, and our methods start with approximating the normal component of the magnetic field on the mesh skeleton. For the Cartesian mesh considered here, these are $B_{x,h}^{n+1,C}$ along y-direction element interfaces and $B_{y,h}^{n+1,C}$ along x-direction element interfaces. To this end, we discretize two *one-dimensional* equations in (7)

$$\frac{\partial B_x}{\partial t} = -\frac{\partial E_z}{\partial y}, \quad \frac{\partial B_y}{\partial t} = \frac{\partial E_z}{\partial x} \tag{16}$$

with respect to the primal mesh $\mathcal{T}_h^C$: for any i, j, one looks for $b_x^{i,j}(y) \in P^k(y_j, y_{j+1})$ and $b_y^{i,j}(x) \in P^k(x_i, x_{i+1})$, such that

$$\int_{y_j}^{y_{j+1}} b_x^{i,j}(y)\mu(y) dy = \int_{y_j}^{y_{j+1}} \left(\theta_n B_{x,h}^{n,D}(x_i, y) + (1 - \theta_n)B_{x,h}^{n,C}(x_i, y)\right)\mu(y) dy$$
$$+ \Delta t_n \left(\int_{y_j}^{y_{j+1}} E_z^{n,D}(x_i, y)\frac{\partial \mu(y)}{\partial y} dy - E_{z,i,j+1}^{n,D}\mu(y_{j+1}) + E_{z,i,j}^{n,D}\mu(y_j)\right), \tag{17}$$

for any $\mu(y) \in P^k(y_j, y_{j+1})$, and

$$\int_{x_i}^{x_{i+1}} b_y^{i,j}(x)v(x)dx = \int_{x_i}^{x_{i+1}} \left(\theta_n B_{y,h}^{n,D}(x,y_j) + (1-\theta_n)B_{y,h}^{n,C}(x,y_j)\right)v(x)dx$$
$$+ \Delta t_n \left(-\int_{x_i}^{x_{i+1}} E_z^{n,D}(x,y_j)\frac{\partial v(x)}{\partial x}dx + E_{z,i+1,j}^{n,D}v(x_{i+1}) - E_{z,i,j}^{n,D}v(x_i)\right), \tag{18}$$

for any $v(x) \in P^k(x_i, x_{i+1})$, where $E_z^{n,D}(x,y) = E_z\left(\mathbf{U}_h^{n,D}(x,y), \mathcal{B}_h^{n,D}(x,y)\right)$ and $E_{z,i,j}^{n,D} = E_z^{n,D}(x_i, y_j)$ for any i and j, and θ_n is the same as before. Here $b_x^{i,j}$ and $b_y^{i,j}$ approximate $B_x(x_i, y)$ for $y \in (y_j, y_{j+1})$ and $B_y(x, y_j)$ for $x \in (x_i, x_{i+1})$ at t_{n+1}, respectively, and they were used in [20] to reconstruct an exactly divergence-free magnetic field $\mathcal{B}_h^{n,C}$ of the second order accuracy when $k = 1$ and of the third order accuracy when $k = 2$. However for $k > 2$, since $\left\{b_x^{i,j}, b_y^{i,j}\right\}_{i,j}$ are defined only on mesh skeleton, they alone are insufficient to reconstruct a function in $\mathcal{M}^{C,k}$ which is defined on the whole domain Ω. In order to extract more information about $\mathcal{B}$, we revisit (7) as a real d-dimensional system of equations instead of a set of one dimensional problems on the mesh skeleton, and discretize it using the standard central DG method of relatively *lower* order accuracy. More specifically, for $k \geqslant 2$, we look for $\widetilde{\mathcal{B}} \in \mathcal{V}_h^{C,k-2}$ such that for any $\mathbf{v} = (v_1, v_2)^{\mathrm{T}}$ in $\mathcal{V}_h^{C,k-2}|_{C_{i,j}} = [P^{k-2}(C_{i,j})]^d$ with any i, j,

$$\int_{C_{i,j}} \widetilde{\mathcal{B}} \cdot \mathbf{v}d\mathbf{x} = \int_{C_{i,j}} \left(\theta_n \mathcal{B}_h^{n,D} + (1-\theta_n)\mathcal{B}_h^{n,C}\right) \cdot \mathbf{v}d\mathbf{x} - \Delta t_n \left(\int_{C_{i,j}} E_z^{n,D}(\frac{\partial v_2}{\partial x} - \frac{\partial v_1}{\partial y})d\mathbf{x} + \int_{\partial C_{i,j}} E_z^{n,D}(n_2 v_1 - n_1 v_2)ds\right), \tag{19}$$

where $(n_1, n_2)^{\mathrm{T}}$ is the outward pointing unit normal vector along $\partial C_{i,j}$. It is assumed here and later $[P^r(K)]^d = \{0\}$ for any negative integer r. In fact if the trial and test spaces above are replaced with $\mathcal{V}_h^{C,k}$, the scheme with (15) and the modified (19) is just the $(k+1)$ st order central DG method in [24] applied to the ideal MHD system. In our algorithm, only the P^{k-2} part of that numerical magnetic field is needed. With $\left\{b_x^{i,j}, b_y^{i,j}\right\}_{i,j}$ from (17) and (18) and $\widetilde{\mathcal{B}}$ from (19), we are now ready to introduce an element-by-element reconstruction which defines $\mathcal{B}_h^{n+1,C} = \left(B_{x,h}^{n+1,C}, B_{y,h}^{n+1,C}\right)$ for an *arbitrary* index $k \geqslant 0$.

Reconstruction. Given i and j, reconstruct $\mathcal{B}_h^{n+1,C}|_{C_{i,j}} \in \mathcal{W}^k(C_{i,j})$ such that $\mathcal{B}_h^{n+1,C} = \left(B_{x,h}^{n+1,C}, B_{y,h}^{n+1,C}\right)$ satisfying

(i) $B_{x,h}^{n+1,C}(x_l, y) = b_x^{l,j}(y)$ for $l = i, i+1$ and $y \in (y_j, y_{j+1})$.
(ii) $B_{y,h}^{n+1,C}(x, y_l) = b_y^{i,l}(x)$ for $l = j, j+1$ and $x \in (x_i, x_{i+1})$.
(iii) For $k \geqslant 2$, there is also $\int_{C_{i,j}} \left(\mathcal{B}_h^{n+1,C} - \widetilde{\mathcal{B}}\right) \cdot \mathbf{v}d\mathbf{x} = 0, \forall \mathbf{v} \in [P^{k-2}(C_{i,j})]^d$.

One can see that the normal component of the reconstructed magnetic field $\mathcal{B}_h^{n+1,C}$ across element interfaces is given either by $b_x^{i,j}$ or $b_y^{i,j}$ with some index i and j. The remaining degrees of freedom of $\mathcal{B}_h^{n+1,C}$ when $k \geqslant 2$ are determined by $\widetilde{\mathcal{B}}$ in such a way that the L^2 projection of $\mathcal{B}_h^{n+1,C}$ onto $\mathcal{V}_h^{C,k-2}$ is exactly $\widetilde{\mathcal{B}}$. The main results for the reconstruction are summarized in next Theorem, with its proof given in Section 4.

Theorem 3.1. *For any $k \geqslant 0$,*

($\mathcal{R}1$) $\mathcal{B}_h^{n+1,C}|_{C_{i,j}} \in \mathcal{W}^k(C_{i,j})$ *is uniquely determined.*
($\mathcal{R}2$) $\nabla \cdot \mathcal{B}_h^{n+1,C}|_{C_{i,j}} = 0$, *and therefore $\mathcal{B}_h^{n+1,C} \in \mathcal{M}^{C,k}$ and it is exactly divergence-free.*
($\mathcal{R}3$) *When $k = 1, 2$, the reconstructions are the same as those in [20].*

Remark 3.2

(1) To define the reconstruction, we have used Property 1 in Lemma 2.1. In fact, (i) and (ii) are equivalent to

(i) For $l = i, i+1$, $\int_{y_j}^{y_{j+1}} \left(B_{x,h}^{n+1,C}(x_l, y) - b_x^{l,j}(y)\right)w(y)dy = 0, \forall w \in P^k(y_j, y_{j+1})$.

(ii) For $l = j, j+1$, $\int_{x_i}^{x_{i+1}} \left(B_{y,h}^{n+1,C}(x, y_l) - b_y^{i,l}(x)\right)w(x)dx = 0, \forall w \in P^k(x_i, x_{i+1})$.

These equivalent formulations were used in [8] when BDM elements were introduced.
(2) Theorem 3.1 implies that the local reconstruction procedure defined above produces an exactly divergence-free magnetic field $\mathcal{B}_h^{n+1,C}$. The index $k \geqslant 0$ can be arbitrary. Not like in other divergence-free reconstruction strategies, such as in [4,22,20] where the reconstructed magnetic field being divergence-free is part of the definition of the reconstruction, in our reconstruction, this is a derived property.

4. Proof of Theorem 3.1

The following Lemma provides a key relation of $\left\{b_x^{i,j}\right\}_{i,j}$, $\left\{b_y^{i,j}\right\}_{i,j}$ and $\widetilde{\mathcal{B}}$. It is related to

$$\int_{\partial K} \mathbf{V} \cdot \mathbf{n} w ds = \int_K \nabla \cdot \mathbf{V} w d\mathbf{x} + \int_K \mathbf{V} \cdot \nabla w d\mathbf{x}, \tag{20}$$

an equality derived from the divergence theorem, and it ensures the reconstructed magnetic field to be divergence-free.

Lemma 4.1 (*Relation of* $\left\{b_x^{i,j}\right\}_{i,j}$, $\left\{b_y^{i,j}\right\}_{i,j}$ *and* $\widetilde{\mathcal{B}}$). *For any* $w \in P^{k-1}(C_{i,j})$, *there is*

$$\int_{\partial C_{i,j}} \Theta \cdot \mathbf{n} w ds = \begin{cases} \int_{C_{i,j}} \widetilde{\mathcal{B}} \cdot \nabla w d\mathbf{x}, & k > 1, \\ 0, & k = 1. \end{cases} \tag{21}$$

Here

$$\int_{\partial C_{i,j}} \Theta \cdot \mathbf{n} w ds := \int_{y_j}^{y_{j+1}} b_x^{i+1,j}(y) w(x_{i+1}, y) dy - \int_{y_j}^{y_{j+1}} b_x^{i,j}(y) w(x_i, y) dy + \int_{x_i}^{x_{i+1}} b_y^{i,j+1}(x) w(x, y_{j+1}) dx - \int_{x_i}^{x_{i+1}} b_y^{i,j}(x) w(x, y_j) dx. \tag{22}$$

Proof. For any $w \in P^{k-1}(C_{i,j})$ with $k \geqslant 1$, by taking the test function in (17) and (18) to be w, we have

$$
\begin{aligned}
\int_{\partial C_{i,j}} \Theta \cdot \mathbf{n} w ds &= \int_{y_j}^{y_{j+1}} b_x^{i+1,j}(y) w(x_{i+1}, y) - b_x^{i,j}(y) w(x_i, y) dy + \int_{x_i}^{x_{i+1}} b_y^{i,j+1}(x) w(x, y_{j+1}) - b_y^{i,j}(x) w(x, y_j) dx \\
&= \int_{y_j}^{y_{j+1}} \left(\theta_n B_{x,h}^{n,D}(x_{i+1}, y) + (1 - \theta_n) B_{x,h}^{n,C}(x_{i+1}, y) \right) w(x_{i+1}, y) dy \\
&\quad + \Delta t_n \left(\int_{y_j}^{y_{j+1}} E_z^{n,D}(x_{i+1}, y) \frac{\partial w(x_{i+1}, y)}{\partial y} dy - E_{z,i+1,j+1}^{n,D} w_{i+1,j+1} + E_{z,i+1,j}^{n,D} w_{i+1,j} \right) \\
&\quad - \int_{y_j}^{y_{j+1}} \left(\theta_n B_{x,h}^{n,D}(x_i, y) + (1 - \theta_n) B_{x,h}^{n,C}(x_i, y) \right) w(x_i, y) dy \\
&\quad - \Delta t_n \left(\int_{y_j}^{y_{j+1}} E_z^{n,D}(x_i, y) \frac{\partial w(x_i, y)}{\partial y} dy - E_{z,i,j+1}^{n,D} w_{i,j+1} + E_{z,i,j}^{n,D} w_{i,j} \right) \\
&\quad + \int_{x_i}^{x_{i+1}} \left(\theta_n B_{y,h}^{n,D}(x, y_{j+1}) + (1 - \theta_n) B_{y,h}^{n,C}(x, y_{j+1}) \right) w(x, y_{j+1}) dx \\
&\quad - \Delta t_n \left(\int_{x_i}^{x_{i+1}} E_z^{n,D}(x, y_{j+1}) \frac{\partial w(x, y_{j+1})}{\partial x} dx - E_{z,i+1,j+1}^{n,D} w_{i+1,j+1} + E_{z,i,j+1}^{n,D} w_{i,j+1} \right) \\
&\quad - \int_{x_i}^{x_{i+1}} \left(\theta_n B_{y,h}^{n,D}(x, y_j) + (1 - \theta_n) B_{y,h}^{n,C}(x, y_j) \right) w(x, y_j) dx \\
&\quad + \Delta t_n \left(\int_{x_i}^{x_{i+1}} E_z^{n,D}(x, y_j) \frac{\partial w(x, y_j)}{\partial x} dx - E_{z,i+1,j}^{n,D} w_{i+1,j} + E_{z,i,j}^{n,D} w_{i,j} \right).
\end{aligned} \tag{23}
$$

All terms containing $E_z^{n,D} w$ at vertices are perfectly canceled. With further simplification, one gets

$$
\begin{aligned}
\int_{\partial C_{i,j}} \Theta \cdot \mathbf{n} w ds &= \int_{\partial C_{i,j}} \left(\theta_n \mathcal{B}_h^{n,D} + (1 - \theta_n) \mathcal{B}_h^{n,C} \right) \cdot \mathbf{n} w ds - \Delta t_n \int_{\partial C_{i,j}} E_z^{n,D} \left(\frac{\partial w}{\partial x} n_2 - \frac{\partial w}{\partial y} n_1 \right) ds \\
&= \int_{C_{i,j}} \left(\theta_n \nabla \cdot \mathcal{B}_h^{n,D} + (1 - \theta_n) \nabla \cdot \mathcal{B}_h^{n,C} \right) w d\mathbf{x} + \int_{C_{i,j}} \left(\theta_n \mathcal{B}_h^{n,D} + (1 - \theta_n) \mathcal{B}_h^{n,C} \right) \cdot \nabla w d\mathbf{x} \\
&\quad - \Delta t_n \int_{\partial C_{i,j}} E_z^{n,D} \left(\frac{\partial w}{\partial x} n_2 - \frac{\partial w}{\partial y} n_1 \right) ds \\
&= \int_{C_{i,j}} \left(\theta_n \mathcal{B}_h^{n,D} + (1 - \theta_n) \mathcal{B}_h^{n,C} \right) \cdot \nabla w d\mathbf{x} - \Delta t_n \int_{\partial C_{i,j}} E_z^{n,D} \left(\frac{\partial w}{\partial x} n_2 - \frac{\partial w}{\partial y} n_1 \right) ds. \tag{24}
\end{aligned}
$$

For the last step, we use the fact that both $\mathcal{B}_h^{n,C}$ and $\mathcal{B}_h^{n,D}$ are exactly divergence-free.

When $k = 1$, w is constant on $C_{i,j}$ and its gradient is zero. Therefore $\int_{\partial C_{i,j}} \Theta \cdot \mathbf{n} w ds = 0$, and this gives (21) for $k = 1$.

For $k > 1$, we further take $\mathbf{v} = \nabla w \in [P^{k-2}(C_{i,j})]^d$ in (19), then

$$\int_{C_{i,j}} \widetilde{\mathcal{B}} \cdot \nabla w d\mathbf{x} = \int_{C_{i,j}} \left(\theta_n \mathcal{B}_h^{n,D} + (1 - \theta_n) \mathcal{B}_h^{n,C} \right) \cdot \nabla w d\mathbf{x} - \Delta t_n \int_{\partial C_{i,j}} E_z^{n,D} \left(\frac{\partial w}{\partial x} n_2 - \frac{\partial w}{\partial y} n_1 \right) ds,$$

and this is exactly the same as $\int_{\partial C_{i,j}} \boldsymbol{\Theta} \cdot \mathbf{n} w ds$, hence (21) holds for $k > 1$. □

Remark 4.2

(1) The proof of (21) relies on the use of the same θ_n in (17)–(19). This θ_n can be different from the one in (15), which is not directly related to the reconstruction.

(2) With $w \equiv 1$, (21) becomes

$$\int_{y_j}^{y_{j+1}} b_x^{i+1\,j}(y) dy - \int_{y_j}^{y_{j+1}} b_x^{i\,j}(y) dy + \int_{x_i}^{x_{i+1}} b_y^{i\,j+1}(x) dx - \int_{x_i}^{x_{i+1}} b_y^{i\,j}(x) dx = 0,$$

and this is the compatible condition in [20].

(3) The electric field flux $\{E_{z,i,j}^{n,D}\}_{i,j}$, used to discretize the induction Eqs. (17) and (18), are evaluated based on the numerical solution on the dual mesh, they are single-valued at the grid-points of the primal mesh and therefore all relevant terms are canceled out. For Godunov type methods [5,16,4] under the constrained transport framework, additional interpolation or averaging procedure is required to produce a single-valued electric magnetic flux at the grid-points. Certain upwind mechanism also needs to be incorporated for stability consideration especially for high order schemes.

We are now ready to prove Theorem 3.1 for the proposed reconstruction.

Proof of Theorem 3.1

Step 1. For $(\mathcal{R}1)$, we first prove the result when $k \geqslant 1$ by following [8]. Note that for two dimensions with $d = 2$, the reconstruction of $\mathcal{B}_h^{n+1,C}|_{C_{i,j}}$ involves $4(k + 1) + \dim([P^{k-2}]^d) = 4(k + 1) + d\frac{k(k-1)}{2} = k^2 + 3k + 4$ conditions, which equals to the dimension of $\mathcal{W}^k(C_{i,j})$. Therefore to get $(\mathcal{R}1)$, one only needs to show that with the zero data, namely, $b_x^{i\,j}(y) = b_x^{i+1\,j}(y) = 0$, $b_y^{i\,j}(x) = b_y^{i\,j+1}(x) = 0$, and if $k > 1$ there is also $\widetilde{\mathcal{B}}(x,y)|_{C_{i,j}} = 0$, the reconstructed $\mathcal{B}_h^{n+1,C}|_{C_{i,j}}$ has to be zero. To this end, we denote

$$\mathcal{B}_h^{n+1,C} = \begin{pmatrix} B_{x,h}^{n+1,C} \\ B_{y,h}^{n+1,C} \end{pmatrix} = \begin{pmatrix} w_1 \\ w_2 \end{pmatrix} + a_1 \begin{pmatrix} x^{k+1} \\ -(k+1)\,x^k y \end{pmatrix} + a_2 \begin{pmatrix} (k+1)xy^k \\ -y^{k+1} \end{pmatrix} \tag{25}$$

in $C_{i,j}$ with $w_l(x,y) = \sum_{0 \leqslant r+s \leqslant k} a_{r,s}^{(l)} x^r y^s$. According to (i) in the definition of the reconstruction, and $b_x^{i\,j}$ and $b_x^{i+1\,j}$ being zero, there is

$$B_{x,h}^{n+1,C}(x,y) = \sum_{\substack{0 \leqslant r+s \leqslant k \\ s \neq k}} a_{r,s}^{(1)} x^r y^s + a_1 x^{k+1} + (a_{0,k}^{(1)} + a_2(k+1)x)y^k = 0$$

at $x = x_i$ and x_{i+1}. Since the last term is the only one containing the monomial y^k, it has to be zero and therefore $a_2 = 0$. With a similar argument to $B_{y,h}^{n+1,C}$, one can further show $a_1 = 0$. Now (25) becomes $(w_1, w_2)^T \in [P^k(C_{i,j})]^2$ where w_1 vanishes at x_i, x_{i+1} and w_2 vanishes at y_j, y_{j+1}. This indicates,

- if $k = 1$, (w_1, w_2) has to be zero and so does $\mathcal{B}_h^{n+1,C}|_{C_{i,j}}$.
- if $k > 1$, there is $(w_1, w_2) = ((x - x_i)(x - x_{i+1})\tilde{w}_1, (y - y_j)(y - y_{j+1})\tilde{w}_2)$ with some $(\tilde{w}_1, \tilde{w}_2)^T \in [P^{k-2}(C_{i,j})]^2$. Now we can take $\mathbf{v} = (\tilde{w}_1, \tilde{w}_2)^T$ in (iii) of the reconstruction. With the assumption $\widetilde{\mathcal{B}}(x,y)|_{C_{i,j}} = 0$, one gets $(\tilde{w}_1, \tilde{w}_2) = (0,0)$, and hence $\mathcal{B}_h^{n+1,C}|_{C_{i,j}} = 0$.

Next we want to prove $(\mathcal{R}1)$ when $k = 0$. In this case,

$$\mathcal{B}_h^{n+1,C} = \begin{pmatrix} a_1 \\ a_2 \end{pmatrix} + c \begin{pmatrix} x \\ -y \end{pmatrix} \tag{26}$$

in $C_{i,j}$ for some constants a_1, a_2 and c, and the reconstruction becomes

$$a_1 + c x_{i+1} = b_x^{i+1\,j}, a_1 + c x_i = b_x^{i\,j}, \quad a_2 - c y_{j+1} = b_y^{i\,j+1}, a_2 - c y_j = b_y^{i\,j}. \tag{27}$$

On the other hand, Lemma 4.1 with $w \equiv 1$ for $k = 0$ gives

$$(y_{j+1} - y_j)\left(b_x^{i+1\,j} - b_x^{i\,j} \right) + (x_{i+1} - x_i)\left(b_y^{i\,j+1} - b_y^{i\,j} \right) = 0,$$

which ensures that the system (27) is uniquely solvable, in particular with

$$c = \frac{b_x^{i+1\,j} - b_x^{i\,j}}{x_{i+1} - x_i} = -\frac{b_y^{i\,j+1} - b_y^{i\,j}}{y_{j+1} - y_j}, \quad a_1 = b_x^{i\,j} - c x_i, a_2 = b_y^{i\,j} + c y_j, \tag{28}$$

and therefore the reconstruction is well-defined for $k = 0$.

Step 2. For ($\mathcal{R}2$), we first show that the reconstructed $\mathcal{B}_h^{n+1,C}$ is divergence-free on $C_{i,j}$. For $k = 0$, this comes directly with the explicit formula (26) and (28) of the reconstruction. For $k \geqslant 1$, consider any $w \in P^{k-1}(C_{i,j})$, there is

$$\int_{C_{i,j}} \nabla \cdot \mathcal{B}_h^{n+1,C} w d\mathbf{x} = -\int_{C_{i,j}} \mathcal{B}_h^{n+1,C} \cdot \nabla w d\mathbf{x} + \int_{\partial C_{i,j}} \left(\mathcal{B}_h^{n+1,C} \cdot \mathbf{n} \right) w ds = -\int_{C_{i,j}} \widetilde{\mathcal{B}} \cdot \nabla w d\mathbf{x} + \int_{\partial C_{i,j}} (\boldsymbol{\Theta} \cdot \mathbf{n}) w ds = 0. \quad (29)$$

The last two equalities are due to the definition of the reconstruction and Lemma 4.1. Moreover, Lemma 2.1 implies $\nabla \cdot \mathcal{B}_h^{n+1,C} \in P^{k-1}(C_{i,j})$. With this, one can take $w = \nabla \cdot \mathcal{B}_h^{n+1,C}$ in (29) and gets $\nabla \cdot \mathcal{B}_h^{n+1,C}|_{C_{i,j}} = 0$. Now $\mathcal{B}_h^{n+1,C}|_{C_{i,j}} \in \mathcal{W}^k(C_{i,j})$, it is divergence-free in each mesh element and has continuous normal component across element interfaces, therefore $\mathcal{B}_h^{n+1,C} \in \mathcal{M}^{C,k}$ and it is exactly divergence-free.

Step 3. Finally, we want to prove ($\mathcal{R}3$). That is, for $k = 1$ or $k = 2$, our proposed reconstruction and the one in [20] (also given in Appendix A) are the same. First note that (i) and (ii) in our current reconstruction are the same as (i′) and (ii′) in Appendix A.

Suppose $\mathcal{B}_h^{n+1,C}$ is the reconstructed magnetic field on $C_{i,j}$ based on the current definition. With ($\mathcal{R}2$) proved above, $\nabla \cdot \mathcal{B}_h^{n+1,C}|_{C_{i,j}} = 0$, and therefore this $\mathcal{B}_h^{n+1,C}$ satisfies (i′)–(iii′) in Appendix A.

Suppose $\mathcal{B}_h^{n+1,C}$ is the reconstructed magnetic field on $C_{i,j}$ based on the definition in Appendix A (and also [20]). We only need to show that when $k = 2$, this $\mathcal{B}_h^{n+1,C}$ satisfies (iii) of the current reconstruction. For any $\mathbf{v} = \begin{pmatrix} v_1 \\ v_2 \end{pmatrix} \in [P^{k-2}(C_{i,j})]^d$, one can write it as $\mathbf{v} = \nabla w$ with $w = v_1 x + v_2 y \in P^{k-1}(C_{i,j})$. Based on (21), there is $\int_{\partial C_{i,j}} \boldsymbol{\Theta} \cdot \mathbf{n} w ds = \int_{C_{i,j}} \widetilde{\mathcal{B}} \cdot \nabla w d\mathbf{x}$, where $\int_{\partial C_{i,j}} \boldsymbol{\Theta} \cdot \mathbf{n} w ds$ is defined in (22). With this

$$\int_{C_{i,j}} \left(\mathcal{B}_h^{n+1,C} - \widetilde{\mathcal{B}} \right) \cdot \mathbf{v} d\mathbf{x} = \int_{C_{i,j}} \left(\mathcal{B}_h^{n+1,C} - \widetilde{\mathcal{B}} \right) \cdot \nabla w d\mathbf{x} = -\int_{C_{i,j}} \nabla \cdot \mathcal{B}_h^{n+1,C} w d\mathbf{x} + \int_{\partial C_{i,j}} \mathcal{B}_h^{n+1,C} \cdot \mathbf{n} w ds - \int_{C_{i,j}} \widetilde{\mathcal{B}} \cdot \nabla w d\mathbf{x}$$

$$= -\int_{C_{i,j}} \nabla \cdot \mathcal{B}_h^{n+1,C} w d\mathbf{x} + \int_{\partial C_{i,j}} \boldsymbol{\Theta} \cdot \mathbf{n} w ds - \int_{C_{i,j}} \widetilde{\mathcal{B}} \cdot \nabla w d\mathbf{x} = -\int_{C_{i,j}} \nabla \cdot \mathcal{B}_h^{n+1,C} w d\mathbf{x} = 0.$$

The last equality uses that the reconstructed magnetic field $\mathcal{B}_h^{n+1,C}$ is divergence-free on $C_{i,j}$ due to (iii′) in Appendix A. $\quad \square$

Remark 4.3. The relation (21) is only used to show the reconstructed magnetic field being divergence-free in ($\mathcal{R}2$), and it is not needed for the unique solvability in ($\mathcal{R}1$) of the proposed reconstruction.

5. Further discussion

5.1. Divergence-free discrete spaces

For the numerical methods proposed in Section 3, the divergence-free subspace of a $H(\text{div})$-conforming discrete space, the BDM finite element space, is used to approximate the magnetic field $\mathcal{B}$. Within the current framework, one can also use some other $H(\text{div})$-conforming finite element spaces, such as the Brezzi–Douglas–Fortin–Marini (BDFM) [9] or Raviart–Thomas (RT) [28] finite element spaces. Of all three, the BDM finite element space is the smallest in order to achieve the same order of accuracy in L^2 norm.

5.2. Relation to some other divergence-free methods

Our methods are closely related to [2,4,21,22] among various exactly divergence-free numerical methods in the constrained transport framework for MHD simulations. In all these methods (including ours), one first approximates the normal component $\mathcal{B} \cdot \mathbf{n}$ (or $\mathbf{B} \cdot \mathbf{n}$ in three dimensions) of the magnetic field on mesh interfaces, and then applies a divergence-free reconstruction procedure, with the reconstructed magnetic field having the same normal component on mesh interfaces as obtained in the previous step. Besides the difference in the base methods, such as being finite volume [2,4,21,22] or finite element [20] (and this work) methods, being Godunov [2,4] or central [21,22,20] type, these methods are also different or related in two more aspects: one is in the choice of the discrete spaces the reconstructed magnetic field belongs to; the other is the additional conditions which may be needed to uniquely determine the reconstruction after one matches the normal component on mesh interfaces.

In particular, our reconstruction uses the BDM finite element space, it is the same as the one in [2] for $k = 1$, and for $k = 2$ it is the same as the one in [21]. When $k = 3$, both our method and [22] employ the same discrete space BDM$_k$. While being divergence-free is part of the definition of the reconstruction in [22], it is a derived property of the reconstructed magnetic field in our approach. After one matches the normal component of the magnetic field on mesh interfaces, the additional conditions to ensure the unique solvability of the reconstruction are also quite different. The strategy proposed in our current work relies on extensive use of the magnetic induction equations in order to extract sufficient information about

the magnetic field, it provides reconstructions for *any* integer index $k \geqslant 0$ and results in exactly divergence-free numerical methods of arbitrary order of accuracy. The actual performance of the methods with higher k certainly needs further investigation. The additional conditions in [22] on the other hand are motivated either by using more compact stencil in reconstruction or by better resolving planar, grid-aligned flows. In [4], the divergence-free reconstruction uses different discrete spaces for the magnetic field: when $k = 2$, the space is $BDFM_{k+1}$ [9], and when $k = 3$, a space between BDM_k and $BDFM_{k+1}$ is used. In both cases, the additional conditions to ensure the unique solvability of the reconstruction are motivated by minimizing the magnetic energy. The reconstructions in [4] are given for three dimensions, and the two-dimensional version can be obtained by neglecting the spatial variable z.

It is not easy to see which strategy of [22,4] and our current work is better in terms of accuracy and stability when uniquely determining the reconstruction of exactly divergence-free high order accurate magnetic fields in MHD simulations. This is partially due to the difference in the base methods. Our proposed strategy seems to be a promising candidate as it relies on extensive use of the magnetic induction equations. More analysis is needed to better understand our approach and to evaluate the strength of different strategies.

5.3. High order time discretizations

To achieve better accuracy in time, strong stability preserving (SSP) high order time discretizations [18] can be used. Such discretization can be written as a convex combination of the forward Euler method, and therefore the full scheme with a high order SSP time discretization still produces an exactly divergence-free approximation for the magnetic field. For multi-stage time discretizations such as SSP Runge–Kutta methods, one needs to apply the divergence-free reconstruction for each inner stage.

5.4. Nonlinear limiters

When central DG methods are applied to nonlinear problems such as the ideal MHD system, nonlinear limiters are often needed. In this paper we use the minmod TVB slope limiter in [29,12], which is simple yet involves a nonnegative parameter M. This limiter can be implemented componentwisely or in local characteristic fields. We take $M = 10$ in all numerical simulations in Section 6 whenever the limiter is applied. Different values of M or other limiters [27,23] may produce better results for each individual example, and this will not be explored in this paper.

As in [20], when nonlinear limiter technique is used, it is only applied to **U**, not to $\mathcal{B}$, $\widetilde{\mathcal{B}}$ or $\left(b_x^{i,j}, b_y^{i,j}\right)_{i,j}$. This is to ensure that the property (21) in Lemma 4.1 still holds. Such a strategy may not always be able to effectively control the oscillation in the magnetic field and therefore may affect the numerical stability of the algorithm. Numerical experiments for $k = 3$ in this paper and for $k = 1, 2$ in [20] however indicate that the proposed methods with such limiting strategy perform well when they are applied to many commonly used two-dimensional MHD examples, which include some examples involving a discontinuous magnetic field, such as the Orszag–Tang vortex problem, the rotor problem, and the blast problem.

6. Numerical examples

In this section, we report a set of numerical experiments to illustrate the accuracy and stability of the proposed methods. Except for the first three examples, we only present the numerical results of the fourth order method with $k = 3$. The formulation of the local reconstruction used in this case is given in Appendix B. In all simulations, the primal mesh is Cartesian and uniform with meshsizes Δx and Δy. The third order TVD Runge–Kutta method [12] is used as the time discretization, with the time step dynamically determined by

$$\frac{C_{cfl}}{\left(\dfrac{\max\left(|u_x|+c_f^x\right)}{\Delta x} + \dfrac{\max\left(|u_y|+c_f^y\right)}{\Delta y}\right)}. \tag{30}$$

Here c_f^x and c_f^y are the fast speed in x and y directions, respectively (see [26] for the definition), and the CFL number C_{cfl} is taken as 1.0 for $k = 1$, 0.6 for $k = 2$, and 0.3 for $k = 3$ unless otherwise specified. We use $\theta_n = 1$ in (15) and (17)–(19). When demonstrating the accuracy order for $k = 3$, one needs to reduce the CFL number by a factor c_0 as the mesh is refined in order to match the third order temporal accuracy with the fourth order spatial accuracy. The value of c_0 will be specified below for individual example. All reported results are based on the numerical solutions on the primal mesh. The minmod TVB slope limiter with $M = 10$ is applied to non-smooth examples in order to enhance the numerical stability. One can refer to [20] for more discussion on initialization and boundary conditions.

6.1. Accuracy test

6.1.1. Smooth Alfvén wave
The first example describes a circularly polarized smooth Alfvén wave ([30,21,20]). Following [21], the initial conditions are taken as

$$\rho = 1, \quad u_\parallel = 0, \quad u_\perp = 0.1\sin(2\pi\beta), \quad u_z = 0.1\cos(2\pi\beta),$$
$$B_\parallel = 1, \quad B_\perp = u_\perp, \quad B_z = u_z, \quad p = 0.1,$$

on $\Omega = [0, 1/\cos\alpha] \times [0, 1/\sin\alpha]$. Here $\alpha = \pi/4$ is the angle with respect to the x-axis at which the wave propagates, and $\beta = x\cos\alpha + y\sin\alpha$. The subscripts $\parallel$ and $\perp$ denote the directions parallel and perpendicular to the wave propagation direction, respectively. The boundary conditions are periodic and $\gamma = 5/3$. The Alfvén wave travels at a constant Alfvén speed $B_\parallel/\sqrt{\rho} = 1$ and the solution returns to its initial configuration when t is an integer. In the simulation with $k = 3$, the CFL number C_{cfl} is reduced by a factor $c_0 = 0.5$ when the mesh is refined from $N \times N$ to $N/2 \times N/2$, with the initial C_{cfl} as 0.4. No nonlinear limiter is applied. In Table 1, we report L^2 errors and orders of accuracy for u_x, u_z, B_x and B_z at $t = 2$. The results show that the proposed methods are $(k+1)$ st order accurate when $k = 1, 2, 3$, and they are optimal.

We also want to use this example to illustrate some advantage of high order methods. In our simulations, a third order TVD Runge–Kutta method is applied as the time discretization for $k = 1, 2, 3$. On a given mesh, when k increases, smaller CFL number (hence smaller time step) needs to be taken due to stability consideration, while the computational complexity for one time step increases. It turns out that the increase in the overall computational cost on a given mesh by using higher order methods is paid back by much smaller errors and therefore better solution resolution, and this can be seen from Table 1. In addition, we also report the computational time in the last column of Table 1, and the computational time (horizontal axis) versus L^2 error in Fig. 1 for u_x (left) and u_z (right). The results show that in order to reduce the errors of approximating solutions to a given threshold especially when this threshold is small, it is more cost efficient to work with high order methods. This is consistent to many other studies in literature. Our results are obtained from simulations performed on a computer with 2.27 GHz Intel Core 2 Duo processor and 12 GB DDR3 memory.

6.1.2. Smooth vortex problem

The second example, introduced in [3], describes a smooth vortex propagating at the speed $(1, 1)$ in the two-dimensional domain. The initial conditions are

$$(\rho, u_x, u_y, u_z, B_x, B_y, B_z, p) = (1, 1 + \delta u_x, 1 + \delta u_y, 0, \delta B_x, \delta B_y, 0, 1 + \delta p)$$

with

$$(\delta u_x, \delta u_y) = \frac{\xi}{2\pi}\hat{\nabla} \times \exp\{0.5(1 - r^2)\}, (\delta B_x, \delta B_y) = \frac{\eta}{2\pi}\hat{\nabla} \times \exp\{0.5(1 - r^2)\},$$

and

$$\delta p = \frac{\eta^2(1 - r^2) - \xi^2}{8\pi^2}\exp(1 - r^2).$$

Here $r = \sqrt{x^2 + y^2}$, $\xi = 1$, $\eta = 1$, and $\gamma = 5/3$. In the simulation with $k = 3$, the CFL number C_{cfl} is reduced by a factor $c_0 = (1/2)^{1/3}$ when the mesh is refined from $N \times N$ to $N/2 \times N/2$, with the initial C_{cfl} as 0.3. The computational domain is taken as $[-10, 10] \times [-10, 10]$ with periodic boundary conditions. Such boundary condition treatment introduces an error with the magnitude $O\left(e^{\frac{1-10^2}{2}}\right) = O(10^{-22})$, which is much smaller than the errors we report and therefore will not affect the accuracy

Table 1
L^2 errors, orders of accuracy, and computational time (in seconds) for the smooth Alfvén wave problem at $t = 2$. C_{cfl} is 1.0 for $k = 1$ and 0.6 for $k = 2$. For $k = 3$, C_{cfl} is 0.4 on the initial mesh with a reduction factor $c_0 = 0.5$.

| N	u_x		u_z		B_x		B_z		Time
	L^2 error	Order	L^2 error	Order	L^2 error	Order	L^2 error	Order	
$k = 1$									
16	2.10E−03	–	2.78E−03	–	1.89E−03	–	2.78E−03	–	0.59
32	3.65E−04	2.52	5.02E−04	2.47	2.78E−04	2.76	5.02E−04	2.47	4.76
64	7.74E−05	2.24	1.11E−04	2.18	4.97E−05	2.48	1.11E−04	2.18	40.70
128	1.84E−05	2.07	2.68E−05	2.05	1.09E−05	2.19	2.68E−05	2.05	347.40
$k = 2$									
16	5.97E−04	–	1.22E−04	–	6.05E−04	–	1.23E−04	–	3.67
32	7.31E−05	3.03	1.50E−05	3.03	7.34E−05	3.04	1.50E−05	3.03	29.49
64	9.08E−06	3.01	1.86E−06	3.01	9.09E−06	3.02	1.87E−06	3.01	247.40
128	1.13E−06	3.00	2.33E−07	3.00	1.13E−06	3.01	2.34E−07	3.00	2163.15
$k = 3$									
16	4.23E−05	–	1.80E−05	–	1.28E−05	–	1.81E−05	–	16.60
32	2.57E−06	4.04	4.15E−07	5.44	3.13E−07	5.36	4.19E−07	5.43	269.91
64	1.62E−07	3.98	1.97E−08	4.40	1.57E−08	4.32	1.97E−08	4.41	4521.03
128	1.02E−08	3.99	1.21E−09	4.02	9.69E − 10	4.02	1.21E−09	4.02	73907.58
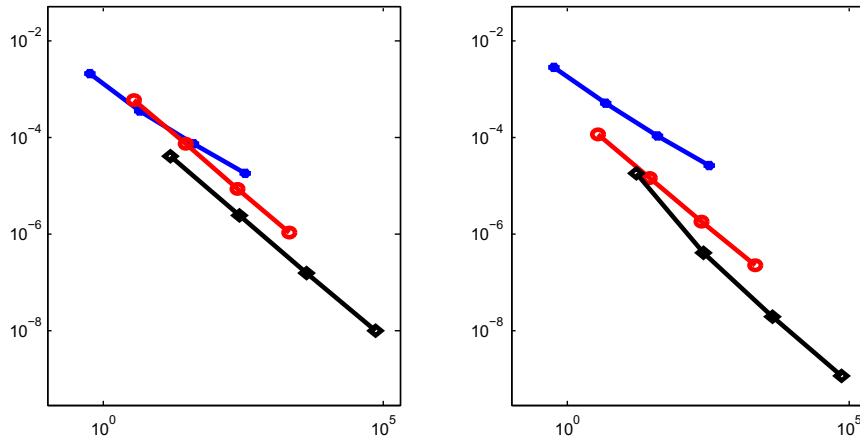
Fig. 1. Computational time (horizontal axis) versus L^2 error in u_x (left) and u_z (right) for the smooth Alfvén wave problem at $t = 2$. From top to bottom: $k = 1$ (solid star in blue), $k = 2$ (circle in red), $k = 3$ (diamond in black). (For interpretation of the references to colour in this figure legend, the reader is referred to the web version of this article.)

Table 2
L^2 errors and orders of accuracy for the smooth vortex example on $[-10, 10] \times [-10, 10]$ at $t = 20$. C_{cfl} is 1.0 for $k = 1$ and 0.6 for $k = 2$. For $k = 3$, C_{cfl} is 0.3 on the initial mesh with a reduction factor $c_0 = (1/2)^{1/3}$.

N	ρ		u_x		B_x		p	
	L^2 error	Order	L^2 error	Order	L^2 error	Order	L^2 error	Order
k = 1								
32	3.33E−03	–	1.23E−01	–	1.22E−01	–	1.87E−02	–
64	1.35E−03	1.28	2.91E−02	2.08	2.82E−02	2.11	5.37E−03	1.80
128	3.22E−04	2.07	4.38E−03	2.74	4.16E−03	2.76	8.80E−04	2.61
256	6.13E−05	2.39	5.97E−04	2.87	5.52E−04	2.91	1.36E−04	2.69
k = 2								
32	7.00E−03	–	2.05E−02	–	6.96E−02	–	9.70E−03	–
64	1.39E−03	2.33	3.75E−03	2.45	1.22E−02	2.51	2.05E−03	2.24
128	1.86E−04	2.90	4.98E−04	2.91	1.61E−03	2.93	2.78E−04	2.88
256	2.34E−05	2.99	6.27E−05	2.99	2.02E−04	2.99	3.51E−05	2.99
k = 3								
32	1.14E−04	–	6.96E−04	–	1.21E−03	–	1.27E−04	–
64	5.83E−06	4.29	3.78E−05	4.20	6.76E−05	4.17	9.54E−06	3.73
128	2.35E−07	4.63	2.01E−06	4.23	2.99E−06	4.50	4.45E−07	4.42
256	1.18E−08	4.31	1.20E−07	4.06	1.45E−07	4.36	2.41E−08	4.21

study. Note that for $k = 1, 2$, a smaller computational domain $[-5, 5] \times [-5, 5]$ with periodic boundary conditions is sufficient and this was used in [20]. In Table 2, we present L^2 errors and orders of accuracy for representative variables ρ, u_x, B_x and p at $t = 20$. The results confirm the optimal accuracy orders of our proposed methods. No nonlinear limiter is applied in the computation.

6.2. Numerical dissipation and long-term decay of Alfvén waves

We next investigate the numerical dissipation of the proposed methods by examining the long-term decay behavior of torsional Alfvén waves, which propagate at a small angle to the y-axis. This problem was tested in [3,22] with various numerical schemes or methods with different accuracy orders. We use the following initial conditions

$$\rho = 1, \quad u_x = -0.2 n_y \cos\phi, \quad u_y = 0.2 n_x \cos\phi, \quad u_z = 0.2 \sin\phi,$$

$$B_x = \frac{n_x}{\sqrt{4\pi}} + 0.2 n_y \cos\phi, \quad B_y = \frac{n_y}{\sqrt{4\pi}} - 0.2 n_x \cos\phi, \quad B_z = -u_z, \quad p = 1.$$

Here $(n_x, n_y) = \left(\frac{1}{\sqrt{r^2+1}}, \frac{r}{\sqrt{r^2+1}} \right)$ is the wave propagation direction, and $\phi = \frac{2\pi}{n_y}(n_x x + n_y y)$ is the initial phase of the wave. The simulation is performed in the domain $\Omega = [-r/2, r/2] \times [-r/2, r/2]$ with $r = 6$. Boundary conditions are periodic and $\gamma = 5/3$.
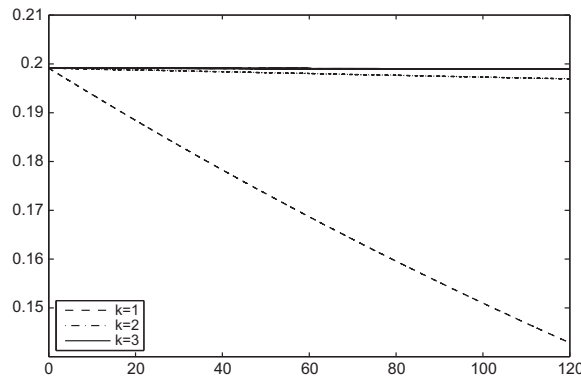
Fig. 2. The temporal evolution of $\max_\Omega |u_z|$ up to $t = 120$ on a 120×120 mesh.

For this example, the maximum values of u_z and B_z are constant in time for the exact solution, yet they will decay in simulations due to numerical dissipation. In Fig. 2, we present the temporal evolution of the maximum value of u_z, $\max_\Omega |u_z|$, up to $t = 120$ for $k = 1, 2, 3$, and the mesh is 120×120. Only the results for u_z is presented as it has a similar decay rate as B_z. Apparently, the fourth order scheme ($k = 3$) has the smallest numerical dissipation while the second order scheme ($k = 1$) has the largest. In particular, for the fourth order scheme, the absolute change in $\max_\Omega |u_z|$ is $\max_\Omega |u_z||_{t=0} - \max_\Omega |u_z||_{t=120} = O(10^{-5})$ over such a long time simulation. Moreover, there is significant improvement from the second order scheme to higher than second order schemes, indicating the advantages of using high order methods in controlling numerical dissipation. This has been observed or analyzed for many other high order methods, such as the divergence-free central finite volume methods in [22], and discontinuous Galerkin methods in [11,1]. In Fig. 3, we also present the results for $k = 2$ (left) and $k = 3$ (right) on different meshes: 60×60, 90×90 and 120×120. While the numerical dissipation is smaller for finer grids, it has much less dependence on the meshsizes for higher order methods.

6.3. Orszag–Tang vortex problem

In this subsection, we consider the Orszag–Tang vortex problem which is a widely used test example in MHD simulations. The initial conditions are taken as [19,20]

$$\rho = \gamma^2, \quad u_x = -\sin y, \quad u_y = \sin x, \quad u_z = 0,$$
$$B_x = -\sin y, \quad B_y = \sin 2x, \quad B_z = 0, \quad p = \gamma,$$

with $\gamma = 5/3$. The computational domain is $[0, 2\pi] \times [0, 2\pi]$ with periodic boundary conditions. The solution involves formation and interaction of multiple shocks as the nonlinear system evolves, and this can be seen from the time evolution of density ρ in Fig. 4. The computation is carried out with $k = 3$ on a 192×192 mesh.

Numerical evidence in [19,22] suggests that insufficient treatment of the divergence-free condition may affect the numerical stability for this example. For instance, the DG method with the P^2 approximation breaks down in the simulation, and this is partially overcome when the locally divergence-free DG method with the same accuracy is used [19]. With our exactly divergence-free central DG methods, the numerical simulation can continue stably for $k = 1, 2$ [20] and for $k = 3$ up to $t = 30$ (the maximum time we run, and the simulation can still go on).

We further perform a qualitative convergence study for this example. In Fig. 5, we plot pressure p (left) with $y = 1.9635$ at $t = 2$ using meshes 192×192 and 384×384, and $k = 3$. With shocks developed in the solution at this time, convergence can be observed, and the pressure slices are almost the same as the second and third order exactly divergence-free central DG approximations in [20] and the locally divergence-free DG approximations in [19]. The reported results are computed with the nonlinear limiter implemented in the local characteristic fields. Though this limiter is applied only to $\mathbf{U}_h$, there is no significant oscillation in numerical solutions, see Fig. 5 (right) for the numerical B_x with $x = \pi$ at $t = 3$. Finally, we want to point out that no negative pressure is encountered throughout the simulation.

6.4. Rotor problem

Next we consider the rotor problem which was explained in greater details in [5]. The problem describes a dense disk of fluid rapidly spinning in a light ambient fluid. Following [30,20], the starting setup is given as

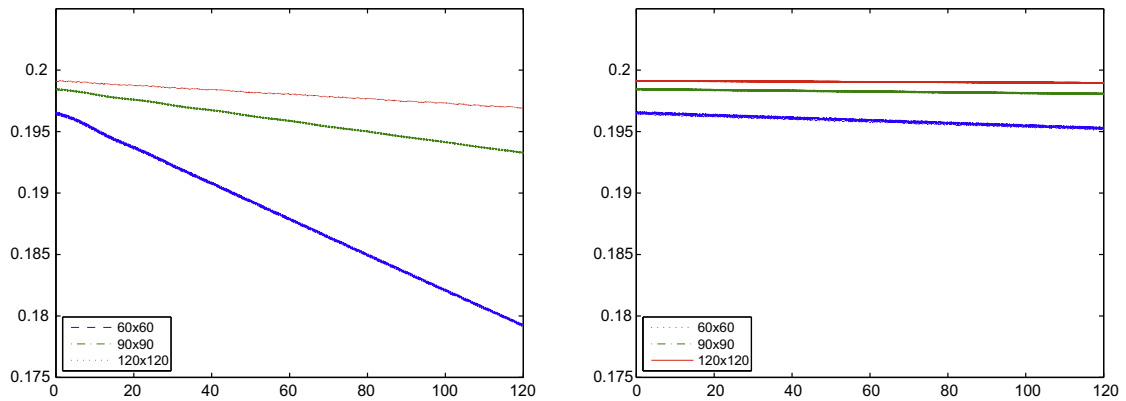$$(u_z, B_x, B_y, B_z, p) = (0, 2.5/\sqrt{4\pi}, 0, 0, 0.5),$$

and

Fig. 3. The temporal evolution of $\max_\Omega |u_z|$ up to $t = 120$ with $k = 2$ (left) and $k = 3$ (right) on various meshes.
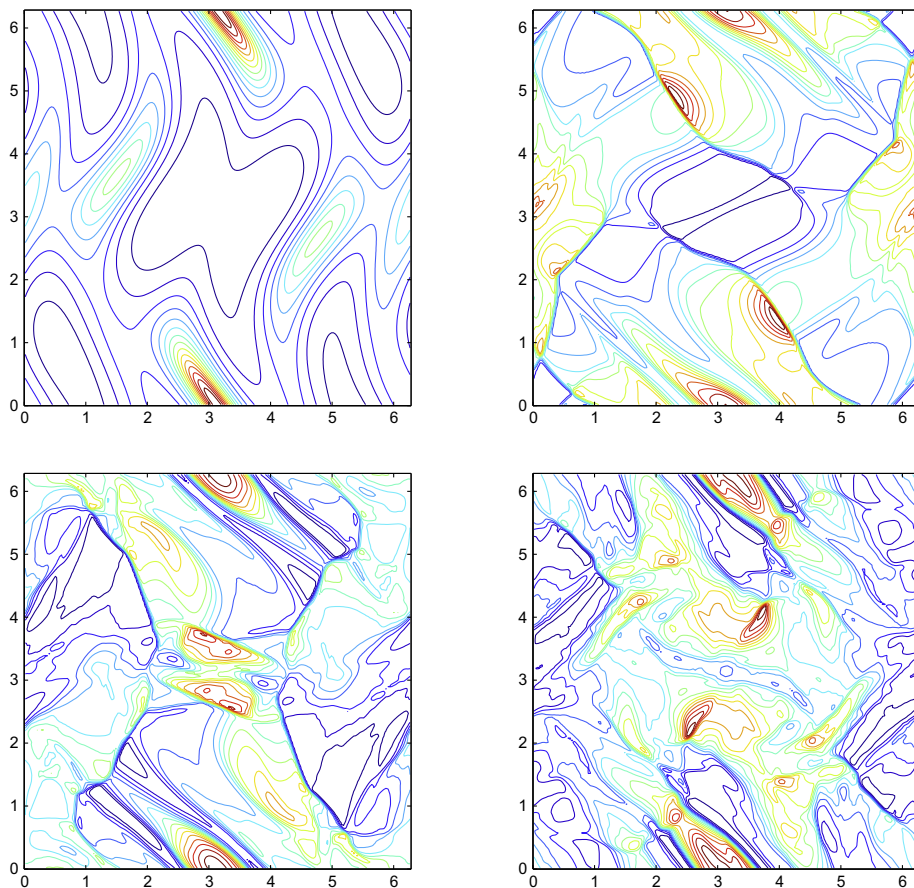

Fig. 4. Density ρ in Orszag–Tang vortex problem at $t = 0.5$ (top left), $t = 2$ (top right), $t = 3$ (bottom left), and $t = 4$ (bottom right), with $k = 3$ on a 192×192 mesh. Fifteen equally spaced contours with ranges [2.11,5.84], [0.62,6.25],[1.25, 6.03], and [1.28,5.71], respectively.

$$
(\rho, u_x, u_y) = \begin{cases} (10, -(y - 0.5)/r_0, (x - 0.5)/r_0 & \text{if } r < r_0, \\ (1 + 9\lambda, -\lambda(y - 0.5)/r, \lambda(x - 0.5)/r) & \text{if } r_0 < r < r_1, \\ (1, 0, 0) & \text{if } r > r_1, \end{cases}
$$

with $r = \sqrt{(x - 0.5)^2 + (y - 0.5)^2}$, $r_0 = 0.1$, $r_1 = 0.115$ and $\lambda = (r_1 - r)/(r_1 - r_0)$. The simulation is implemented in the domain $[0,1] \times [0,1]$, and periodic boundary conditions are used with $\gamma = 5/3$. The nonlinear limiter is applied in local
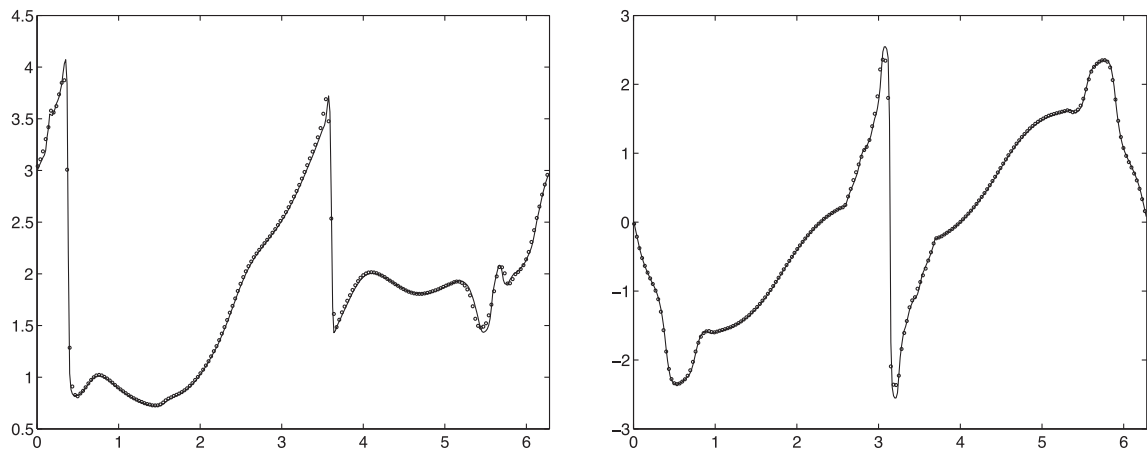
Fig. 5. Orszag–Tang vortex problem with $k = 3$ on 192×192 (circle) and 384×384 (solid line) meshes. Left: p with $y = 1.9635$ at $t = 2$; right: B_x with $x = \pi$ at $t = 3$.

characteristic fields. It turns out that nonlinear limiters are necessary in this example when $k = 3$ for numerical stability, though our methods without limiters produce satisfactory results for $k = 1$ and $k = 2$, see [20].

Similar to [5,30,19,20], in Fig. 6 we examine the performance of the methods by zooming in the central part of the Mach number $|\mathbf{u}|/c$ (with $c = \sqrt{\gamma p / \rho}$ as the sound speed) at $t = 0.295$. Note that there is no "distortion" in the numerical solutions, and such distortion was reported in [30,19] and it was attributed to the divergence error in the magnetic field. We further perform a qualitative convergence study for our method. In Fig. 7, Mach number is presented with $x = 0.413$ and $k = 3$ on 400×400, 600×600 and 800×800 meshes. With several shocks developed in the solution, the convergence of the method is observed, and the solutions slices are almost the same as the second and third order exactly divergence-free central DG approximations in [20] and the locally divergence-free DG approximations in [19]. Though the nonlinear limiter is applied only to $\mathbf{U}_h$ in the simulation, there is no significant oscillation in numerical solutions, see Fig. 8 for B_x with $x = 0.25$ and B_y at $y = 0.5$. These slices are chosen from the region where the magnetic field displays more interesting features. It was reported in [30] that many one step TVD based schemes failed for this problem due to the negative pressure, in our simulation, there is no negative pressure observed.

6.5. Blast problem

The blast wave problem was introduced in [5], and the solution involves strong magnetosonic shocks. We employ the same initial condition as in [5,21,20], that is, $(\rho, u_x, u_y, u_z, B_x, B_y, B_z) = (1, 0, 0, 0, 100/\sqrt{4\pi}, 0, 0)$. The pressure is taken as $p = 1000$ if $r \leqslant R$, and $p = 0.1$ otherwise, where $r = \sqrt{x^2 + y^2}$ and $R = 0.1$. With this setup, the fluid in the region outside the initial pressure pulse has very small plasma $\beta \left(= \frac{p}{(B_x^2 + B_y^2)/2} = 2.513E - 04 \right)$. The simulation is implemented in the domain $[-0.5, 0.5] \times [-0.5, 0.5]$ with a 200×200 mesh and $k = 3$. Outgoing boundary conditions are used, and $\gamma = 1.4$.

In Fig. 9, we present the numerical results at $t = 0.01$ for density ρ, pressure p, square of the total velocity $u_x^2 + u_y^2$, and the magnetic pressure $B_x^2 + B_y^2$. As pointed out in [5,21], this is a stringent problem to solve. Negative pressure is generated near the shock front in our simulation, and this is also observed in many other methods which are not positivity preserving (see e.g. [21]). In Fig. 10 we plot the negative part of pressure $\min(0, p)$. Note that at $t = 0.01$, the minimum value of pressure for $k = 3$ is -3.225 which is slightly smaller than -1.633, the minimum value of pressure of the third order approximation (with $k = 2$ when $M = 1$ is used in the minmod TVB slope limiter) in [20]. In fact, in all cases with $k = 1, 2, 3$, the magnitude of the negative pressure is fairly small for this low plasma β example, and this illustrates the good performance of the proposed methods.

We further report solution slices for ρ and $\sqrt{u_x^2 + u_y^2}$ along $y = 0.0$ in Fig. 11, and for B_x along $x = 0.0$ and B_y along $y = 0.25$ in Fig. 12 on 200×200 and 400×400 meshes. These slices are chosen from the region where the considered field displays more interesting features. The scheme performs well in convergence along with mesh refinement. In addition, there is no significant oscillation observed though the nonlinear limiter is only applied to $\mathbf{U}_h$. For this example, the componentwise TVB minmod limiter is applied. Since we only explicitly use pressure to determine the time step from (30), when negative pressure occurs, $\max(p, \epsilon)$ with $\epsilon = 10^{-5}$ is used to replace p in order to estimate the maximum wave speed in (30). This simple fix results in stable simulation during the time of our interest. When the limiters are implemented in local characteristic fields, the stability of the simulations suffers from the numerical pressure being negative. It is expected that positivity preserving techniques will be very important for this example to ensure the numerical stability, and this is currently under investigation in a separate project.
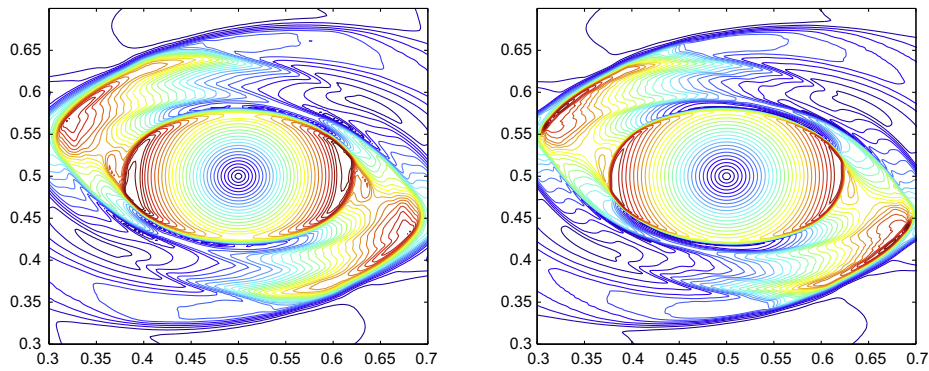
Fig. 6. Zoom-in central part of Mach number in rotor problem at $t = 0.295$ with $k = 3$. Thirty equally spaced contours on a 400×400 mesh with the range of $[0, 2.703]$ (left), and on a 800×800 mesh with the range of $[0, 3.005]$ (right).
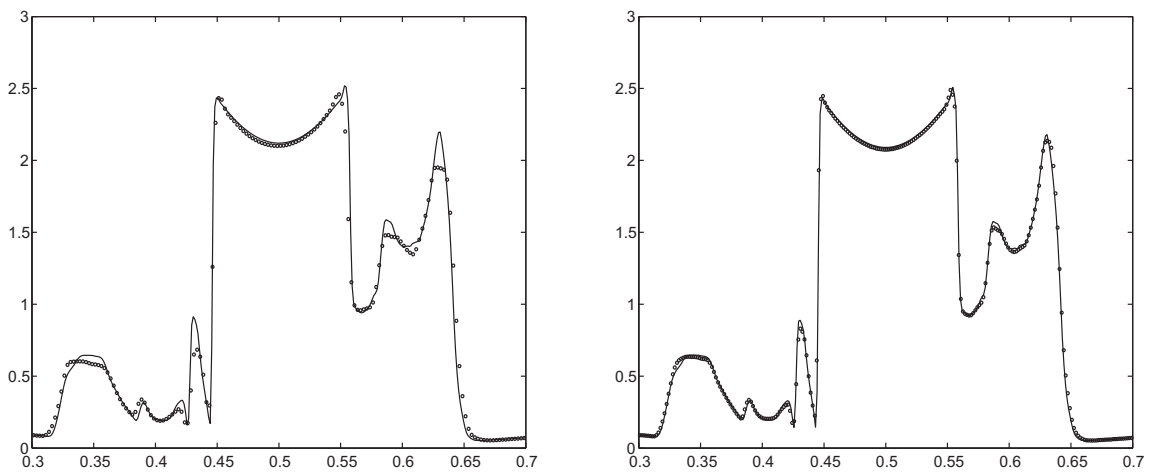

Fig. 7. Mach number in rotor problem at $t = 0.295$ with $x = 0.413$ and $k = 3$. Left: 400×400 (circle) and 800×800 (solid line) meshes; Right: 600×600 (circle) and 800×800 (solid line) meshes.
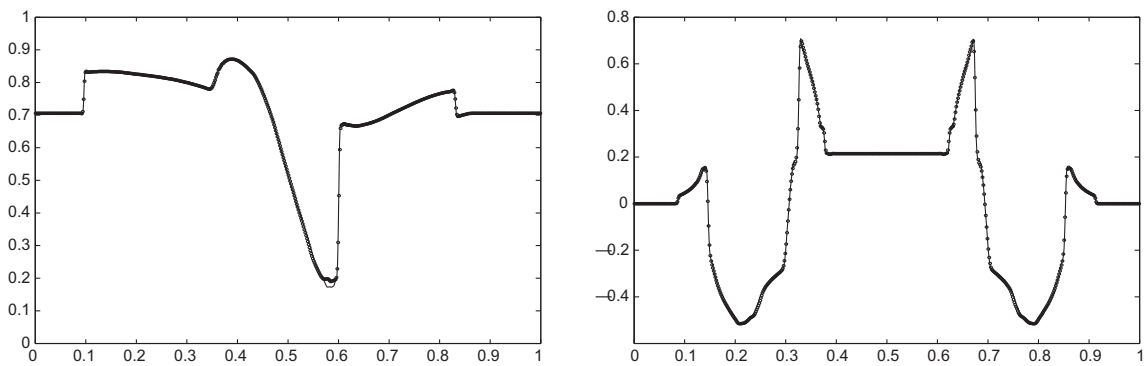
Fig. 8. The magnetic field in rotor problem at $t = 0.295$ with $k = 3$ on 600×600 (circle) and 800×800 (solid line) meshes. Left: B_x with $x = 0.25$; right: B_y with $y = 0.5$.

6.6. Cloud–shock interaction

The last example we consider is the cloud–shock interaction problem which involves strong MHD shocks interacting with a dense cloud. We define three sets of data for $(\rho, u_x, u_y, u_z, B_x, B_y, B_z, p)$,
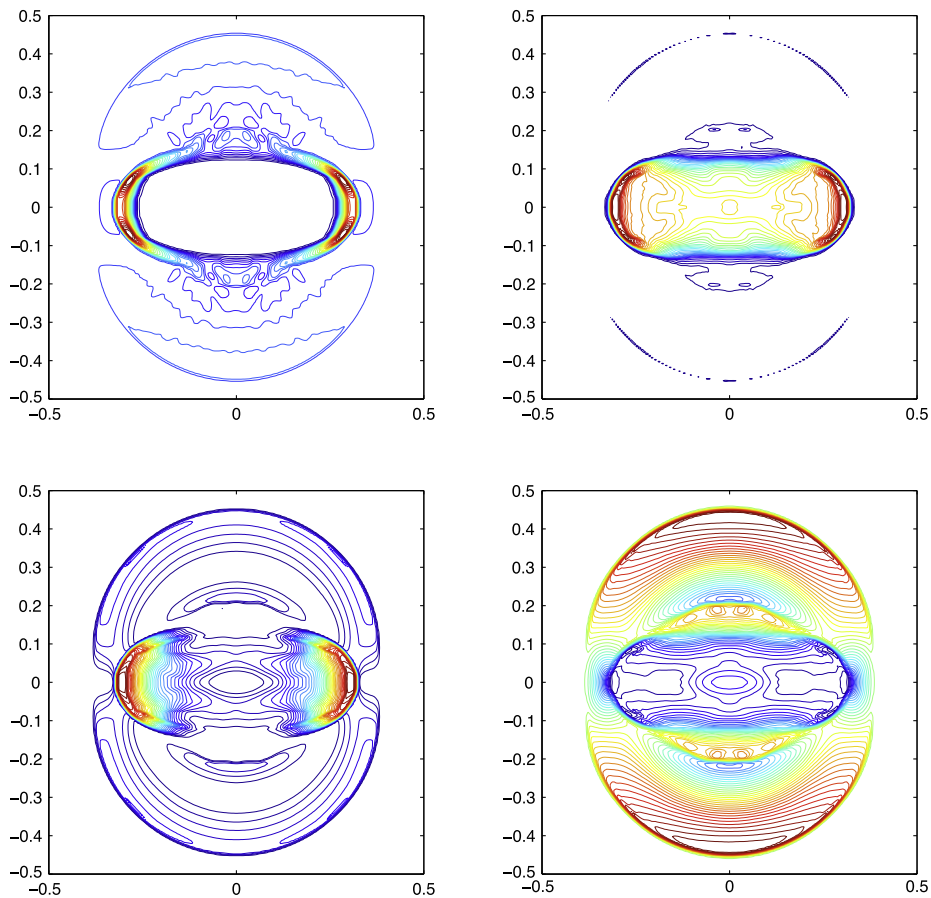
Fig. 9. The blast problem on a 200×200 mesh at $t = 0.01$ with $k = 3$. Forty equally spaced contours are used. Top left: density $\rho \in [0.206, 4.602]$; Top right: pressure $p \in [-3.225, 253.552]$; Bottom left: square of total velocity $u_x^2 + u_y^2 \in [0, 281.680]$; Bottom right: magnetic pressure $B_x^2 + B_y^2 \in [417.365, 1180.984]$.
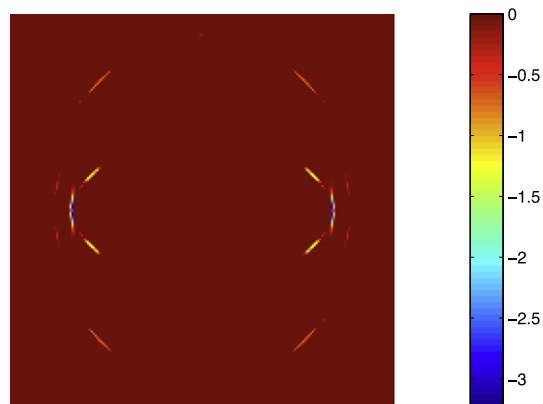

Fig. 10. Negative part of the pressure min $(0, p)$ in the blast problem with $k = 3$ on a 200×200 mesh at $t = 0.01$.

$$\mathbf{U}_1 = (3.88968, 0, 0, -0.05234, 1, 0, 3.9353, 14.2614),$$
$$\mathbf{U}_2 = (1, -3.3156, 0, 0, 1, 0, 1, 0.04), \quad \mathbf{U}_3 = (5, -3.3156, 0, 0, 1, 0, 1, 0.04).$$

The computational domain $[0, 2] \times [0, 1]$ is divided into three regions: the post-shock region $\Omega_1 = \{(x, y) : 0 \leqslant x \leqslant 1.2,$
$0 \leqslant y \leqslant 1\}$, the pre-shock region $\Omega_2 = \{(x, y) : 1.2 < x \leqslant 2, 0 \leqslant y \leqslant 1, \sqrt{(x - 1.4)^2 + (y - 0.5)^2} \geqslant 0.18\}$, and the cloud region
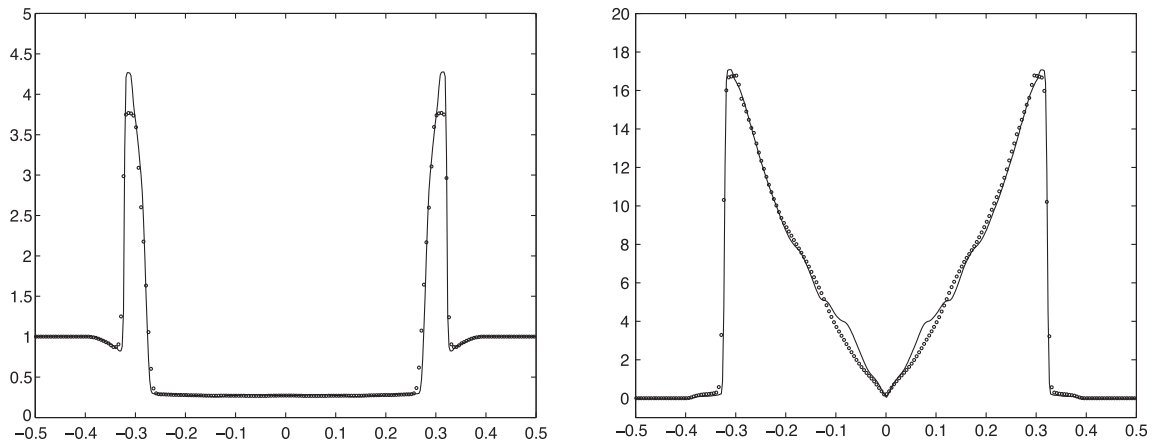
Fig. 11. The blast problem at $t = 0.01$ with $k = 3$ and $y = 0.0$ on 200×200 (circle) and 400×400 (solid line) meshes. Left: ρ; right: $\sqrt{u_x^2 + u_y^2}$.
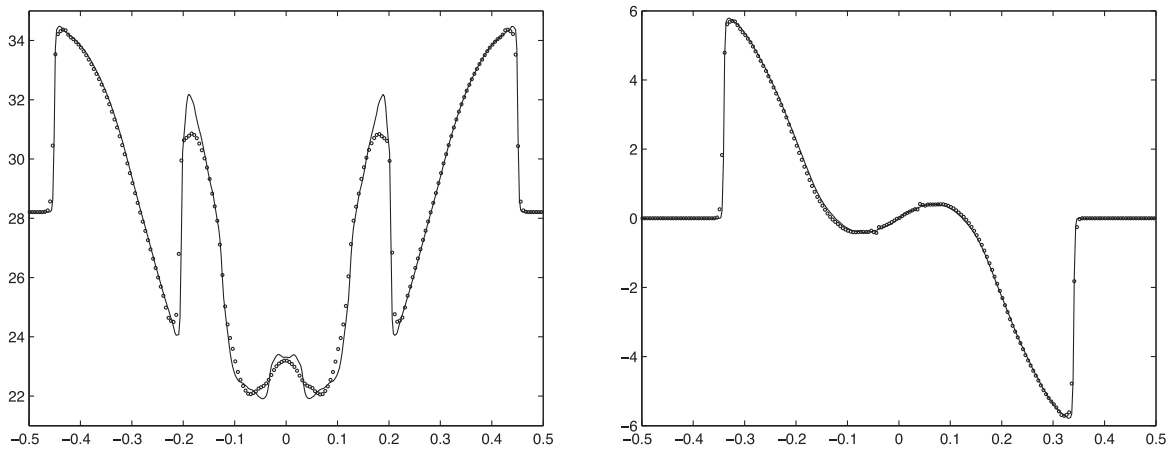

Fig. 12. The blast problem at $t = 0.01$ with $k = 3$ on 200×200 (circle) and 400×400 (solid line) meshes. Left: B_x with $x = 0.0$; right: B_y with $y = 0.25$.
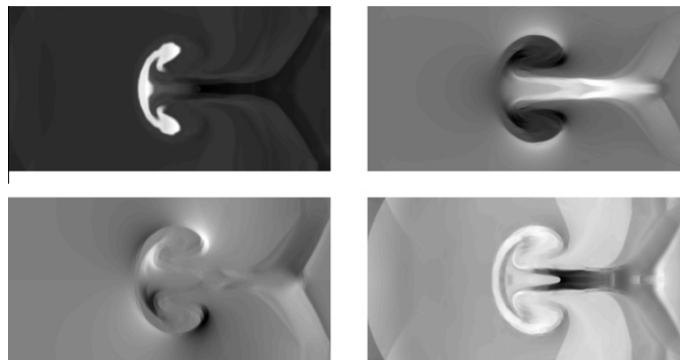

Fig. 13. Gray-scaled images in the cloud–shock interaction problem with $k = 3$ on a 600×300 mesh at $t = 0.6$. Top left: $\rho \in [1.853, 10.678]$; Top right: $B_x \in [-1.750, 4.131]$; bottom left: $B_y \in [-2.723, 2.723]$; bottom right: $p \in [6.536, 14.672]$.

$\Omega_3 = \{(x, y) : \sqrt{(x - 1.4)^2 + (y - 0.5)^2} < 0.18\}$, where the solutions are initialized as $\mathbf{U}_1$, $\mathbf{U}_2$, and $\mathbf{U}_3$, respectively. Note that the cloud is five times denser than its surrounding. Outgoing boundary conditions are used, and $\gamma = 5/3$.
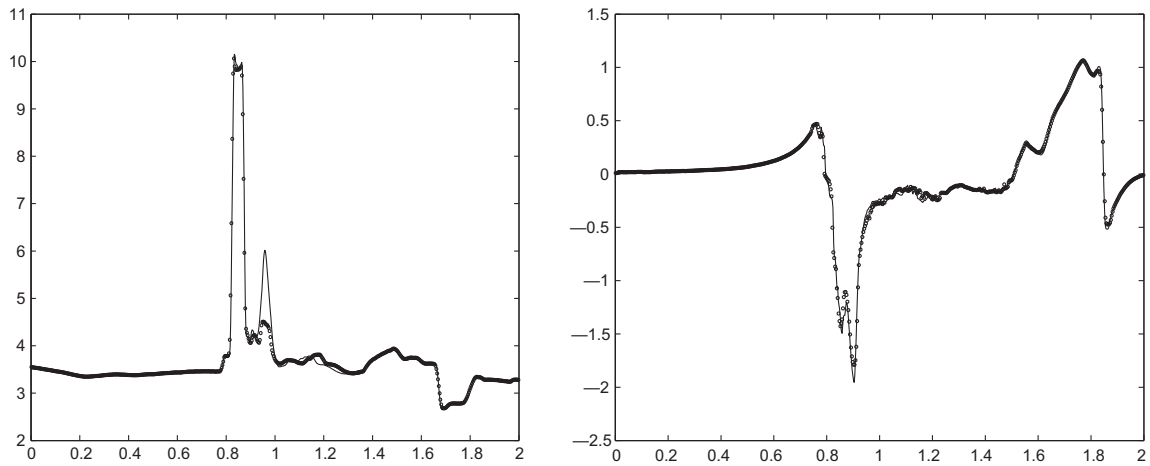
Fig. 14. Cloud–shock interaction problem with $k = 3$ on 600×300 (circle) and 800×400 (solid line) meshes at $t = 0.6$. Left: ρ with $y = 0.6$; right: B_y with $y = 0.59$.

Fig. 13 shows the gray-scale images of density ρ, the magnetic field B_x and B_y, and pressure p at $t = 0.6$ on the mesh 600×300 with $k = 3$. The darker area represents relatively smaller value. In Fig. 14, we also plot the density ρ along $y = 0.6$ and B_y along $y = 0.59$ on 600×300 and 800×400 meshes. Note the main features in Figs. 13 and 14 (left) are the same as the third order approximations in [20], yet with some difference in local details. There is no significant oscillation in the solution, given that the limiter is only applied to $\mathbf{U}_h$. For this example, the nonlinear limiter is implemented in local characteristic fields. We would like to mention that this cloud–shock example is not the same as the one in [13] as different scalings are used in the MHD system for the magnetic field (see our Eqs. (1)–(4) and theirs on page 486 in [13]).

7. Concluding remarks

In this paper, exactly divergence-free central discontinuous Galerkin methods of *arbitrary* order of accuracy are proposed for ideal MHD equations in two dimensions on Cartesian meshes. With the exactly divergence-free magnetic field, the methods demonstrate good stability with designed accuracy. In our ongoing and future projects, we will extend the methods to three dimensions and investigate the numerical performance of the methods with higher order accuracy. In the end, we want to mention that when the standard central DG methods [24] are applied to the whole ideal MHD system without any special discretization for the magnetic induction Eq. (7), the methods perform well for smooth examples and for some non-smooth examples such as Orszag–Tang vortex problem and blast example, but not for all problems. This will be reported in a separate paper [31].

Acknowledgments

Appendix A. Definition of reconstruction in [20]

Reconstruction [20]. Given i and j, reconstruct $\mathcal{B}_h^{n+1,C}|_{C_{ij}} \in \mathcal{W}^k(C_{ij})$ such that $\mathcal{B}_h^{n+1,C} = (B_{x,h}^{n+1,C}, B_{y,h}^{n+1,C})$ satisfying

(i′) $B_{x,h}^{n+1,C}(x_l, y) = b_x^{l,j}(y)$ for $l = i,\ i+1$ and $y \in (y_j, y_{j+1})$.
(ii′) $B_{y,h}^{n+1,C}(x, y_l) = b_y^{i,l}(x)$ for $l = j,\ j+1$ and $x \in (x_i, x_{i+1})$.
(iii′) $\nabla \cdot \mathcal{B}_h^{n+1,C}|_{C_{ij}} = 0$.

Here $b_x^{i,j}(y), b_x^{i+1,j}(y), b_y^{i,j}(x), b_y^{i,j+1}(x)$ are computed according to (17) and (18). This reconstruction is uniquely solvable and therefore well-defined for $k = 1$ and 2.

Appendix B. Formulas of the fourth order reconstruction

In this section, we include explicit formulas of the divergence-free reconstruction defined in Section 3.2 when $k = 3$ without providing the detailed derivation. Given $C = (x_L, x_R) \times (y_L, y_R)$, with $(\bar{x}, \bar{y}) = \left(\frac{x_L + x_R}{2}, \frac{y_L + y_R}{2}\right)$, $\Delta x = x_R - x_L$, $\Delta y = y_R - y_L$, $X = \frac{x - \bar{x}}{\Delta x/2}$ and $Y = \frac{y - \bar{y}}{\Delta y/2}$. Given $b_x^\pm(y) \in P^k(y_L, y_R)$, $b_y^\pm(x) \in P^k(x_L, x_R)$, and $\widetilde{\mathcal{B}} = (\widetilde{B}_x, \widetilde{B}_y)^{\mathrm{T}} \in [P^{k-2}(C)]^2$, with

$$b_x^\pm(y) = a_0^\pm + a_1^\pm Y + a_2^\pm Y^2 + a_3^\pm Y^3, \quad \widetilde{B}_x(x, y) = \tilde{a}_0 + \tilde{a}_1 X + \tilde{a}_2 Y,$$
$$b_y^\pm(x) = b_0^\pm + b_1^\pm X + b_2^\pm X^2 + b_3^\pm X^3, \quad \widetilde{B}_y(x, y) = \tilde{b}_0 + \tilde{b}_1 X + \tilde{b}_2 Y,$$

the reconstruction is to look for $\mathcal{B} = (B_x, B_y)^{\mathrm{T}} \in \mathcal{W}^k(C)$ such that

(1) $B_x(x_L, y) = b_x^-(y), B_x(x_R, y) = b_x^+(y), \forall y \in (y_L, y_R)$.
(2) $B_y(x, y_L) = b_y^-(x), B_y(x, y_R) = b_y^+(x), \forall x \in (x_L, x_R)$.
(3) $\int_C (\mathcal{B} - \widetilde{\mathcal{B}}) \cdot \mathbf{v} d\mathbf{x} = 0, \forall \mathbf{v} \in [P^{k-2}(C)]^2$.

This reconstruction is uniquely determined, and it is given by

$$B_x(x, y) = a_0 + a_1 X + a_2 Y + a_3 X^2 + a_4 XY + a_5 Y^2 + a_6 X^3 + a_7 X^2 Y + a_8 XY^2 + a_9 Y^3 + a_{10} X^4 + a_{11} XY^3,$$

$$B_y(x, y) = b_0 + b_1 X + b_2 Y + b_3 X^2 + b_4 XY + b_5 Y^2 + b_6 X^3 + b_7 X^2 Y + b_8 XY^2 + b_9 Y^3 + b_{10} X^3 Y + b_{11} Y^4,$$

where

$$b_4 = \frac{1}{2}(b_1^+ - b_1^-), \quad a_4 = \frac{1}{2}(a_1^+ - a_1^-),$$

$$b_3 = \frac{1}{2}(b_2^+ + b_2^-), \quad a_5 = \frac{1}{2}(a_2^+ + a_2^-),$$

$$b_7 = \frac{1}{2}(b_2^+ - b_2^-), \quad a_8 = \frac{1}{2}(a_2^+ - a_2^-),$$

$$b_6 = \frac{1}{2}(b_3^+ + b_3^-), \quad a_9 = \frac{1}{2}(a_3^+ + a_3^-),$$

$$b_{10} = -4a_{10}\frac{\Delta y}{\Delta x} = \frac{1}{2}(b_3^+ - b_3^-), \quad a_{11} = -4b_{11}\frac{\Delta x}{\Delta y} = \frac{1}{2}(a_3^+ - a_3^-),$$

$$a_3 = \frac{3}{2}\left(\frac{1}{2}(a_0^+ + a_0^-) + \frac{1}{3}a_5 - \frac{4}{5}a_{10} - \tilde{a}_0\right), \quad a_0 = \frac{1}{2}(a_0^+ + a_0^-) - a_{10} - a_3,$$

$$a_6 = \frac{5}{2}\left(\frac{1}{2}(a_0^+ - a_0^-) + \frac{1}{3}a_8 - \tilde{a}_1\right), \quad a_1 = \frac{1}{2}(a_0^+ - a_0^-) - a_6,$$

$$a_7 = \frac{3}{2}\left(\frac{1}{2}(a_1^+ + a_1^-) + \frac{3}{5}a_9 - \tilde{a}_2\right), \quad a_2 = \frac{1}{2}(a_1^+ + a_1^-) - a_7,$$

$$b_5 = \frac{3}{2}\left(\frac{1}{2}(b_0^+ + b_0^-) + \frac{1}{3}b_3 - \frac{4}{5}b_{11} - \tilde{b}_0\right), \quad b_0 = \frac{1}{2}(b_0^+ + b_0^-) - b_{11} - b_5,$$

$$b_9 = \frac{5}{2}\left(\frac{1}{2}(b_0^+ - b_0^-) + \frac{1}{3}b_7 - \tilde{b}_2\right), \quad b_2 = \frac{1}{2}(b_0^+ - b_0^-) - b_9,$$

$$b_8 = \frac{3}{2}\left(\frac{1}{2}(b_1^+ + b_1^-) + \frac{3}{5}b_6 - \tilde{b}_1\right), \quad b_1 = \frac{1}{2}(b_1^+ + b_1^-) - b_8.$$

Note that b_{10} and a_{10} are interrelated, so are a_{11} and b_{11}. This reconstruction is well-defined for any set of functions $b_x^\pm(y) \in P^k(y_L, y_R)$, $b_y^\pm(x) \in P^k(x_L, x_R)$, and $\widetilde{\mathcal{B}} \in [P^{k-2}(C)]^2$. Furthermore, it is divergence-free when the relation (21) in Lemma 4.1 is satisfied, namely

$$\int_{y_L}^{y_R} b_x^+(y)w(x_R, y)dy - \int_{y_L}^{y_R} b_x^-(y)w(x_L, y)dy + \int_{x_L}^{x_R} b_y^+(x)w(x, y_R)dx - \int_{x_L}^{x_R} b_y^-(x)w(x, y_L)dx = \int_C \widetilde{\mathcal{B}} \cdot \nabla w d\mathbf{x}, \quad \forall w \in P^{k-1}(C),$$

and this is the case for $b_x^\pm(y)$, $b_y^\pm(x)$, and $\widetilde{\mathcal{B}}$ provided by our proposed methods.

On the other hand, if one uses the fact that the reconstructed magnetic field $\mathcal{B} = (B_x, B_y)$ has zero divergence in the proposed framework, many more pairs of coefficients turn out to be interrelated. With this, we can get an alternative set of formulas for the reconstruction,

$$a_4 = -2b_5 \frac{\Delta x}{\Delta y} = \frac{1}{2}\left(a_1^+ - a_1^-\right), \quad b_3 = \frac{1}{2}\left(b_2^+ + b_2^-\right),$$

$$b_4 = -2a_3 \frac{\Delta y}{\Delta x} = \frac{1}{2}\left(b_1^+ - b_1^-\right), \quad a_5 = \frac{1}{2}\left(a_2^+ + a_2^-\right),$$

$$a_8 = -3b_9 \frac{\Delta x}{\Delta y} = \frac{1}{2}\left(a_2^+ - a_2^-\right), \quad b_6 = \frac{1}{2}\left(b_3^+ + b_3^-\right),$$

$$b_7 = -3a_6 \frac{\Delta y}{\Delta x} = \frac{1}{2}\left(b_2^+ - b_2^-\right), \quad a_9 = \frac{1}{2}\left(a_3^+ + a_3^-\right),$$

$$b_2 = -a_1 \frac{\Delta y}{\Delta x} = \frac{1}{2}\left(b_0^+ - b_0^-\right) - b_9,$$

$$a_7 = -b_8 \frac{\Delta x}{\Delta y} = \frac{3}{2}\left(\frac{1}{2}\left(a_1^+ + a_1^-\right) + \frac{3}{5}a_9 - \tilde{a}_2\right),$$

$$b_{10} = -4a_{10} \frac{\Delta y}{\Delta x} = \frac{1}{2}\left(b_3^+ - b_3^-\right), \quad a_2 = \frac{1}{2}\left(a_1^+ + a_1^-\right) - a_7,$$

$$a_{11} = -4b_{11} \frac{\Delta x}{\Delta y} = \frac{1}{2}\left(a_3^+ - a_3^-\right), \quad b_1 = \frac{1}{2}\left(b_1^+ + b_1^-\right) - b_8,$$

$$a_0 = \frac{1}{2}\left(a_0^+ + a_0^-\right) - a_3 - a_{10}, \quad b_0 = \frac{1}{2}\left(b_0^+ + b_0^-\right) - b_5 - b_{11}.$$

For this set, one can also use the following equivalent formulas for a_1, b_2, a_7 and b_8

$$a_1 = -b_2 \frac{\Delta x}{\Delta y} = \frac{1}{2}\left(a_0^+ - a_0^-\right) - a_6,$$

$$b_8 = -a_7 \frac{\Delta y}{\Delta x} = \frac{3}{2}\left(\frac{1}{2}\left(b_1^+ + b_1^-\right) + \frac{3}{5}b_6 - \tilde{b}_1\right).$$

Note that in the formulas based on $\mathcal{B} = (B_x, B_y)$ being divergence-free, among all coefficients of $(\widetilde{B}_x, \widetilde{B}_y)$, only $\tilde{a}_2$ or $\tilde{b}_1$ is needed in the reconstruction. One can utilize this property to improve the implementation efficiency in actual simulation.

References

[1] M. Ainsworth, Dispersive and dissipative behaviour of high order discontinuous Galerkin finite element methods, Journal of Computational Physics 198 (2004) 106–130.
[2] D.S. Balsara, Divergence-free adaptive mesh refinement for magnetohydrodynamics, Journal of Computational Physics 174 (2001) 614–648.
[3] D.S. Balsara, Second order accurate schemes for magnetohydrodynamics with divergence-free reconstruction, Astrophysical Journal Supplement Series 151 (2004) 149–184.
[4] D.S. Balsara, Divergence-free reconstruction of magnetic fields and WENO schemes for magnetohydrodynamics, Journal of Computational Physics 228 (2009) 5040–5056.
[5] D.S. Balsara, D.S. Spicer, A staggered mesh algorithm using high order Godunov fluxes to ensure solenoidal magnetic fields in magnetohydrodynamic simulations, Journal of Computational Physics 149 (1999) 270–292.
[6] T. Barth, On the role of involutions in the discontinuous Galerkin discretization of Maxwell and magnetohydrodynamic systems, in: Arnold, Bochev, Shashkov (Eds.), The IMA Volumes in Mathematics and its Applications, IMA Volume on Compatible Spatial Discretizations, vol. 142, 2005, pp. 69–88.
[7] J.U. Brackbill, D.C. Barnes, The effect of nonzero $\nabla \cdot B$ on the numerical solution of the magnetohydrodynamic equations, Journal of Computational Physics 35 (1980) 426–430.
[8] F. Brezzi, J. Douglas Jr., L.D. Marini, Two families of mixed finite elements for second order elliptic problems, Numerische Mathematik 47 (1985) 217–235.
[9] F. Brezzi, J. Douglas Jr., M. Fortin, L.D. Marini, Efficient rectangular mixed finite elements in two and three space variables, Mathematical Modelling and Numerical Analysis 21 (1987) 581–604.
[10] B. Cockburn, F. Li, C.-W. Shu, Locally divergence-free discontinuous Galerkin methods for the Maxwell equations, Journal of Computational Physics 194 (2004) 588–610.
[11] B. Cockburn, C.-W. Shu, Runge–Kutta discontinuous Galerkin methods for convection-dominated problems, Journal of Scientific Computing 16 (2001) 173–261.
[12] B. Cockburn, C.-W. Shu, The Runge–Kutta discontinuous Galerkin method for conservation laws V: Multidimensional systems, Journal of Computational Physics 141 (1998) 199–224.
[13] W. Dai, P.R. Woodward, Extension of the piecewise parabolic method to multidimensional ideal magnetohydrodynamics, Journal of Computational Physics 115 (1994) 485–514.
[14] A. Dedner, F. Kemm, D. Kröner, C.-D. Munz, T. Schnitner, M. Wesenberg, Hyperbolic divergence cleaning for the MHD equations, Journal of Computational Physics 175 (2002) 645–673.
[15] C.R. Evans, J.F. Hawley, Simulation of magnetohydrodynamic flows: a constrained transport method, Astrophysical Journal 332 (1988) 659–677.
[16] T.A. Gardiner, J.M. Stone, An unsplit Godunov method for ideal MHD via constrained transport, Journal of Computational Physics 205 (2005) 509–539.
[17] S.K. Godunov, Symmetric form of the equations of magnetohydrodynamics, Numerical Methods for Mechanics of Continuum Medium 1 (1972) 26–34.
[18] S. Gottlieb, C.-W. Shu, E. Tadmor, Strong stability preserving high order time discretization methods, SIAM Review 43 (2001) 89–112.
[19] F. Li, C.-W. Shu, Locally divergence-free discontinuous Galerkin methods for MHD equations, Journal of Scientific Computing 22 (2005) 413–442.
[20] F. Li, L. Xu, S. Yakovlev, Central discontinuous Galerkin methods for ideal MHD equations with the exactly divergence-free magnetic field, Journal of Computational Physics 230 (2011) 4828–4847.

[21] S. Li, High order central scheme on overlapping cells for magneto-hydrodynamic flows with and without constrained transport method, Journal of Computational Physics 227 (2008) 7368–7393.
[22] S. Li, A fourth-order divergence-free method for MHD flows, Journal of Computational Physics 229 (2010) 7893–7910.
[23] Y. Liu, C.-W. Shu, E. Tadmor, M. Zhang, Non-oscillatory hierarchical reconstruction for central and finite-volume schemes, Communications in Computational Physics 2 (2007) 933–963.
[24] Y. Liu, C.-W. Shu, E. Tadmor, M. Zhang, Central discontinuous Galerkin methods on overlapping cells with a nonoscillatory hierarchical reconstruction, SIAM Journal on Numerical Analysis 45 (2007) 2442–2467.
[25] Y. Liu, C.-W. Shu, E. Tadmor, M. Zhang, L^2 stability analysis of the central discontinuous Galerkin method and a comparison between the central and regular discontinuous Galerkin methods, ESAIM: Mathematical Modelling and Numerical Analysis 42 (2008) 593–607.
[26] K.G. Powell, An Approximate Riemann Solver for Magnetohydrodynamics (That Works in More than One Dimension), ICASE Report No. 94-24, Langley, VA, 1994.
[27] J. Qiu, C.-W. Shu, Runge–Kutta discontinuous Galerkin method using WENO limiters, SIAM Journal on Scientific Computing 26 (2005) 907–929.
[28] P.-A. Raviart, J.M. Thomas, A mixed finite element method for 2nd order elliptic problems, Mathematical Aspects of Finite Element Methods, Lecture Notes in Mathematics, vol. 60, Springer, Berlin, 1977. pp. 292–315.
[29] C.-W. Shu, TVB uniformly high-order schemes for conservation laws, Mathematics of Computation 49 (1987) 105–121.
[30] G. Tóth, The $\nabla \cdot B = 0$ constraint in shock-capturing magnetohydrodynamics codes, Journal of Computational Physics 161 (2000) 605–652.
[31] S. Yakovlev, L. Xu, F. Li, Locally divergence-free central discontinuous Galerkin methods for ideal MHD equations, submitted for publication.